Monthly Notices
of the
ROYAL ASTRONOMICAL SOCIETY

Mon. Not. R. Astron. Soc. **401,** 1620–1627 (2010) doi:10.1111/j.1365-2966.2009.15787.x

Monte Carlo simulations of the broad-band spectra of Sagittarius A* through the use of general relativistic magnetohydrodynamics

Guy Hilburn,[1,2]★ Edison Liang,[1] Siming Liu[3] and Hui Li[2]

[1]*Department of Physics and Astronomy, Rice University, 6100 Main Street, Houston, Texas 77005, USA*
[2]*Los Alamos National Laboratory, PO Box 1663, Los Alamos, New Mexico 87545, USA*
[3]*Department of Physics and Astronomy, University of Glasgow, Glasgow G12 8QQ*

Accepted 2009 September 28. Received 2009 September 25; in original form 2009 July 14

ABSTRACT

We present results of simulations of the spectrum of the accretion flow on to the supermassive black hole in our Galactic Centre, Sagittarius A*, generated with a coupling of Monte Carlo (MC) radiation and general relativistic magnetohydrodynamic codes. In our modelling, we use the two-dimensional HARM GRMHD code to first model the physical parameters of the disc, then feed its results into our two-dimensional MC photon transport code. We will discuss results obtained which fit radio, infrared and *Chandra*-obtained flaring or quiescent X-ray data points, as well as the validity of the amount of scaling of input parameters (density, temperature and magnetic field) required to fit these points. HARM output will be used to suggest whether the scaling is within reasonable limits.

Key words: accretion, accretion discs – MHD – Galaxy: centre.

1 INTRODUCTION

In recent years, a great deal of effort has been made to understand the complete picture of Sagittarius A* (Sgr A*), a radio/infrared (IR)/X-ray emission source at our Galactic Centre. It is widely accepted that this source is related to the accretion flow of a supermassive black hole whose mass we have taken to be 3.6 million solar masses (Ghez et al. 2003; Melia 2006; Schödel et al. 2007).

The spectrum of Sgr A* shows several important components or signatures. Balick & Brown (1974) first discovered the source in the radio/near-IR, and ensuing observations by a number of researchers confirmed the strength of the source to be primarily in these regimes. Years later, Sgr A*'s X-ray spectrum was explored by Baganoff et al. (2001, 2003), who found notable signatures higher than 10^{17} Hz and also found a variability in this range, which suggests separate spectral states – flaring and quiescent. Simultaneous multiwavelength observations have generally supported this suggestion (Eckart et al. 2004, 2006; Bélanger et al. 2005).

A number of models have arisen to explain the mechanisms at work to produce the spectra of black holes. The standard-disc idea was first explored by Shakura & Sunyaev (1973) and proposes a situation in which gravitational energy is efficiently converted to radiation. This is most appropriate for optically thick discs with the flows on nearly Keplerian orbits. Sgr A*'s luminosity is less than $10^{-8}\,L_{\rm Edd}$, where the Eddington luminosity $L_{\rm Edd}$ represents the luminosity level where the gravitational force inwards equals the radiation force outwards for spherical accretions. Sources with such low luminosities may be described by the standard-disc idea in cases where the disc remains cold and is optically thick, and the luminosity is low primarily due to a very low accretion rate. However, the accretion flow in Sgr A* must be very hot, and there is no evidence for a cold, optically thick disc component. The low luminosity is limited by both a low accretion rate and a low emission efficiency of the flow. In cases such as this, other accretion models need to be considered.

One developed model is called the advection-dominated accretion flow (ADAF) (Ichimaru 1977). This suggested that close to the horizon, much of the energy of the accretion flow was advected into the black hole, rather than being radiated away, and was explored by a number of groups, including Narayan & Yi (1994), Abramowicz et al. (1995) and Yuan, Quataert & Narayan (2003). It was found that the ADAF solution can fit Sgr A* data well (Narayan, Yi & Mahadevan 1995), but, while promising, this approach had several major drawbacks, namely its one-dimensional approach and simplification of magnetic fields. The X-ray emission is produced primarily at large radii, which cannot account for the observed short-time-scale X-ray flares. In an attempt to consider an alternative approach, Yuan et al. (2003) suggested inclusion of non-thermal electrons and found satisfactory fits, but again with simple magnetic fields.

It became apparent that a more complicated treatment of magnetic fields would be important for a more accurate simulation, as the magnetorotational instability (MRI) was found to be of vital importance in the development of turbulence that drives the accretion flow (Hawley 2001; Hawley & Balbus 2002; Balbus 2003). This

★E-mail: guy.l.hilburn@rice.edu

instability ensures that in an accretion disc environment the necessity of outward angular momentum transport leads to the establishment of very complex flow and field patterns.

Models have since begun using magnetohydrodynamic (MHD) codes to simulate accretion flows, with some measure of success. Ohsuga, Kato & Mineshige (2005) ran emission simulations on an MHD model by Kato, Mineshige & Shibata (2004) and were able to fit data well, but had difficulties doing so without cutting out a large portion of their simulation volume. Goldston, Quataert & Igumenshchev (2005) calculated the radio spectrum based on MHD simulations done by Igumenshchev, Narayan & Abramowicz (2003), but not other spectral bands.

We hope to show a simulation method which minimizes compromises on consistency via assumptions or simplifications by using the best tools available to present a more realistic accretion disc picture.

We will present our approach to the Sgr A* modelling using general relativistic magnetohydrodynamic (GRMHD) and Monte Carlo (MC) methods in Section 2, present the results gained through these methods in Section 3 and revisit the most important revelations and conclusions made within in Section 4.

2 SIMULATION METHOD

Our modelling method involves the coupling of two very different codes which complement each other to provide a consistent view of the physical and spectral conditions in the accretion disc of Sgr A*. Detailed in the appropriate sections below are descriptions of the codes, discussions of their appropriateness for our work and the manner in which they were coupled to provide an overall model.

2.1 HARM GRMHD physical space modelling

The GRMHD code selected to determine the model's physical space is the two-dimensional HARM code presented and detailed in Gammie, McKinney & Toth (2003) and Noble et al. (2006). It is not within the scope of this paper to completely detail the HARM code's inner workings, so readers should see these referenced papers for further information.

The code solves hyperbolic partial differential equations in conservative form – uniquely suiting it to a number of astrophysical problems, specifically those involving MHD in areas where general relativity is important. As the code evolves the space through time, conserved variables are converted to primitive variables at each step, to calculate a set of fluxes, given a set of sources. Use of primitive variable calculations allows the code to work with analytic solutions, rather than finding solutions numerically – leading to much faster calculation time.

In this case, the variables tracked include density, total energy, internal energy, flow velocities and magnetic fields. The last two are calculated both as three- and four-component tensor quantities.

2.1.1 Model setup for our work

As imported, HARM was set up quite appropriately for our purposes. It was configured to evolve an accretion disc about a black hole, given a number of user-controlled parameters, on a two-dimensional grid spaced (in spherical coordinates) radially and angularly, and assumed to be axially symmetric about the black hole's spin axis. The cells are assumed to be uniformly spaced with regard to a set of coordinates X1 and X2, which can be converted then to r and θ, respectively. This conversion leads to a logarithmic spacing in r, with cells closer to the horizon having greater resolution (and smaller size) and more concentrated cells closer to the equator. This effectively increases resolution in the plane of the accretion disc and close to the black hole, where the detail is most useful due to the much smaller length-scales of interest in these regions. The resolution increase towards the horizon is vital to the successful running of the code, as it helps to maintain proper cell aspect ratios on the polar grid. A graphical representation of HARM's grid layout can be seen in Fig. 5, where it is compared to the MC code's grid.

As the start, HARM seeds an equilibrium torus around the black hole with density as detailed by Fishbone & Moncrief (1976). The torus is perturbed by adding a small poloidal magnetic field and allowed to evolve around the black hole. We have not attempted runs with an initial toroidal, azimuthal field, though this is allowed by axial symmetry, and should serve to increase the total field at the end of simulation. The additional toroidal component should not influence the MRI development, instead only adding to the final field.

While most default parameters as included are appropriate for the simulation, several had to be tweaked for this project. To effectively simulate conditions near low-luminosity active galactic nuclei, where the non-relativistic gas pressure presumably dominates, an adiabatic index of 5/3 was chosen. As a first approximation, we have chosen a non-spinning black hole. Future work will study the effects of including black hole spin. The simulation volume ranges from just inside the horizon at 2 to 40 GM/c^2 – with the initial torus having an inner radius of 6 GM/c^2 and its pressure maximum at 14.7 GM/c^2. Our final trial was done on a grid of 512×512 – i.e. 512 radial cells by 512 angular cells. Output from the code is all scaled to M, the black hole mass, for near complete freedom.

2.1.2 Results and interpretations

Our simulation was run to approximately 8000 time-steps, which equates to about 1.4×10^5 s, in physical time within the simulation. Fig. 1 displays and explains four panels, which show density, internal energy, squared magnetic field and bulk Lorentz factor through the simulation volume. Of importance to note is that the images are shown evenly spaced in cell number. This creates a kind of stretching effect near the equator and near the horizon – causing the disc to appear much thicker than it actually is.

As expected, the density concentrates itself around the equatorial plane, with the internal energy contours closely following. The magnetic field is strongest in the disc region, but saturates the region, generally being stronger nearer the horizon. More importantly, one can see how highly turbulent the field becomes after being seeded smoothly in the initial torus. As the turbulence is expected to provide the mechanisms for electron heating, in future work, the level to which the field is churned up will be important to analyze. The final panel shows the bulk gas Lorentz factor, which is, as expected, closely related to the distance from the black hole.

Fig. 2 shows profiles of density, temperature and magnetic field along an equatorial slice of the simulation volume. Again of note is the high level of turbulence in the magnetic field. Within 5 GM/c^2, the density and temperature drop to very low levels. This corresponds well with the flow velocities as this is expected to be where the flow becomes almost completely radial, and may be mostly a product of how quickly matter falls to the horizon at this point. Of some concern is how much these final profiles are due to the initial

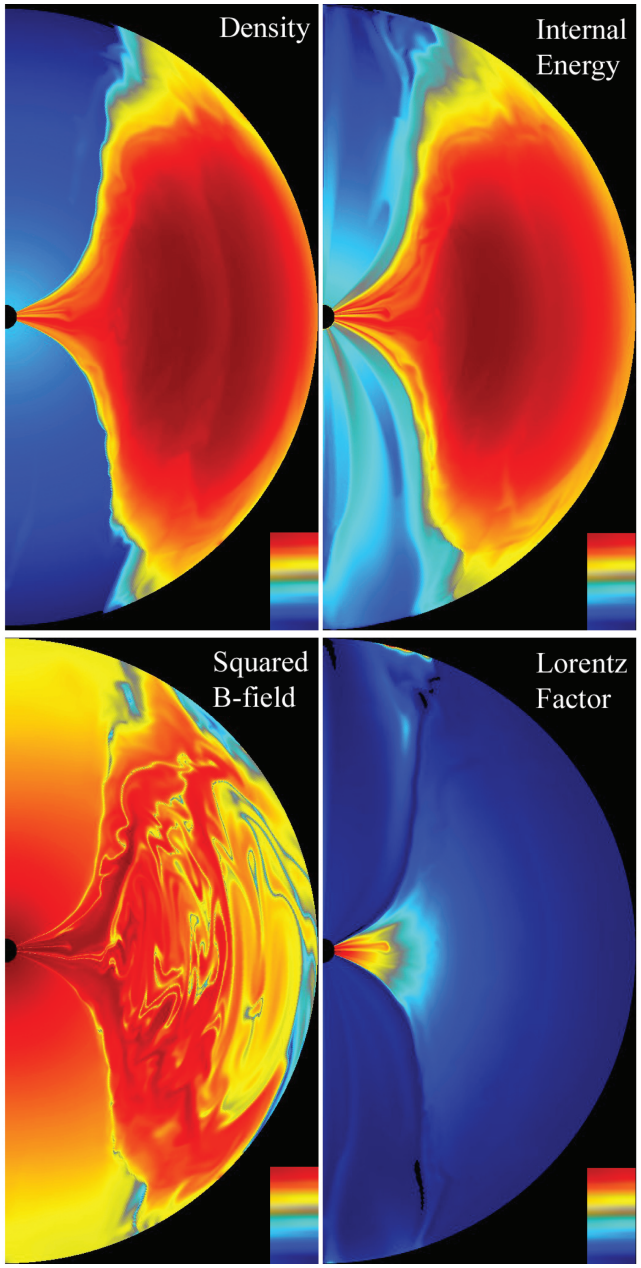

Figure 1. Panels from final time-step $t = 8000$ (1.4×10^5 s) of HARM data, as labelled for different physical quantities. We show a cut-out in the r–z plane, with the black hole's horizon shown on the left. As detailed in the text, the radial direction is scaled logarithmically, and angular dimension is scaled more finely towards the equator. Therefore, the finest resolution is obtained closest to the horizon and equator. This causes a 'spreading' effect in the images, as they are shown evenly spaced by cell number, not physical value. Each quantity is shown on a logarithmic scale, with dark red being the highest values, black being the lowest.

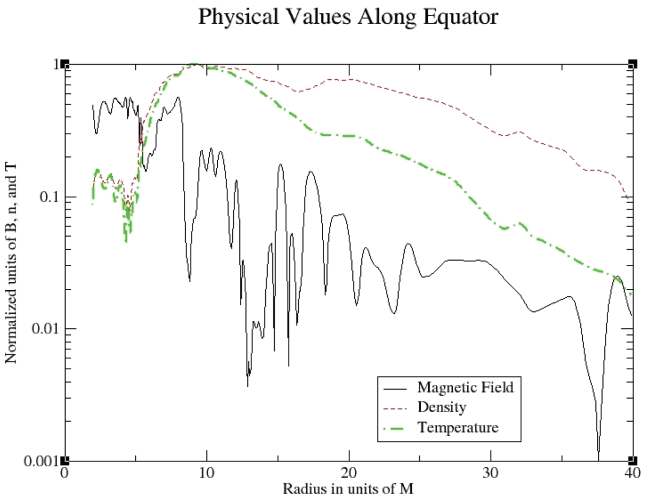

Figure 2. Profiles of magnetic field, density, temperature, along the equator, as a function of radius. These quantities are normalized to the maximum value for each.

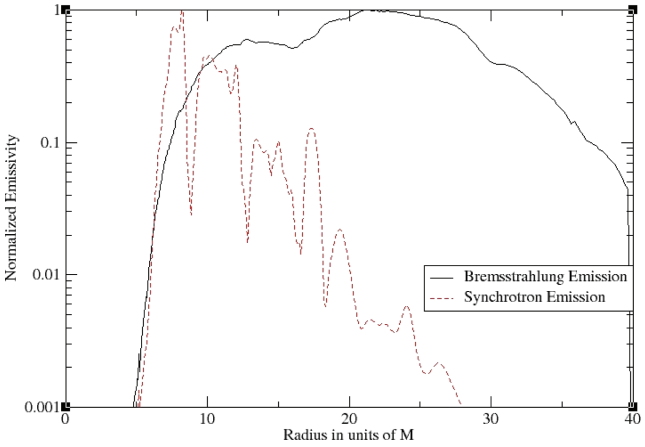

Figure 3. Profiles of optically thin synchrotron and bremsstrahlung emissivity. These values are normalized to the maximum for each set, so no comparisons should be made between the strengths of the two components from this plot. These values are found by determining the emissivity within the closest cell and multiplying it by the radius and scaleheight at that radius.

torus setup. Further trials would be needed to compare initial torus location to final results.

Fig. 3 also shows a profile of the synchrotron and bremsstrahlung emission as a function of radius. To calculate this value, we multiplied the optically thin synchrotron emissivity and bremsstrahlung emissivity, respectively, by the radius and density scaleheight at that radius. The synchrotron emissivity was found by averaging the magnetic field over a number of zones near the equator – this helps to eliminate some of the high variability seen in the magnetic field. It should be noted that the overall shape did not change dramatically as this was averaged over a smaller or larger number of cells. It is apparent that the majority of emission emerges between radii of approximately 8M and 28M. Areas inside and outside this region contribute decreasing amounts to the total emissivity. It is important to note the lack of contribution from the 28M–40M region to overall emission, as our simulation volume for the MC code only extends to 28M (as is discussed below, in relation to the overlap of our two simulation grids).

To demonstrate actual disc thickness, density along a typical slice through a constant radius $r = 9\ GM/c^2$ is shown in Fig. 4.

Our last HARM output figure, Fig. 5, shows the variance of mass accretion on to the black hole through a surface at 28M through time. When comparing parameters required to generate spectra at quiescent and flaring data points, the amount that accretion varies could be important in determining the appropriateness of the variation in values used between the two points. In general, at a late time, mass accretion varies up to a factor of 2. The time-scale of

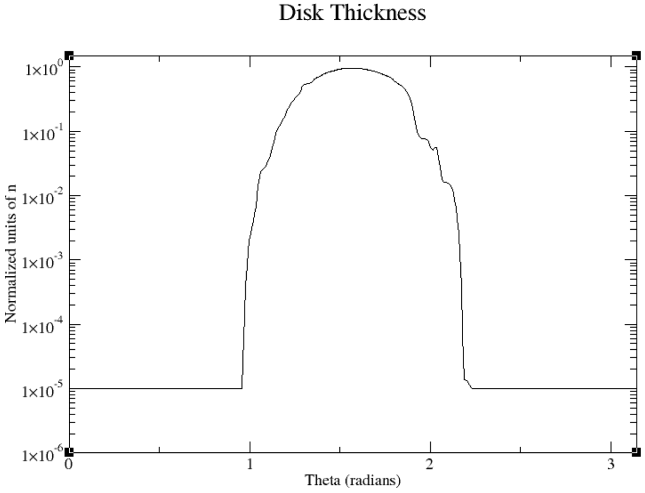

Figure 4. Profile of density along a constant radius $r = 9\ GM/c^2$ slice over θ, from pole to pole. For reference, at this radius, the scaleheight is $2.7\ GM/c^2$.

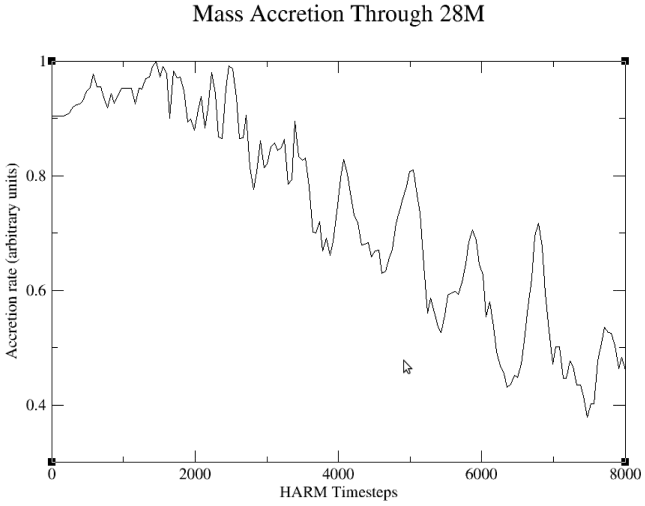

Figure 5. Mass and luminosity accretion rates on to the black hole through a surface at 28M as a function of HARM time-step – with each time-step being equal to approximately 17 physical seconds.

accretion variation, on an order of several hours, is reasonable for the observed variations in Sgr A*'s spectrum. As accretion variation is not only due to instabilities in the flow but also due to changes in density of accreted matter, this factor of 2 is not considered a constraint on scaling.

2.2 Spectrum determination with MC code

The MC code used for photon emission and scattering has a long history and is discussed in a number of resources (Canfield, Howard & Liang 1987; Liang & Dermer 1988; Böttcher & Liang 1998; Böttcher, Liang & Smith 1998; Böttcher & Liang 2001; Böttcher, Jackson & Liang 2003; Finke & Böttcher 2005; Finke 2007). For a complete treatment, readers should see these papers.

In general, this code is a coupled MC/Fokker–Planck (FP) code. For our intents, the FP evolution of the electron distribution was unnecessary at this stage, so it was turned off to allow a fixed temperature given by the HARM output. The code is set up on a two-dimensional axially symmetric cylindrical grid, creating a (hollow

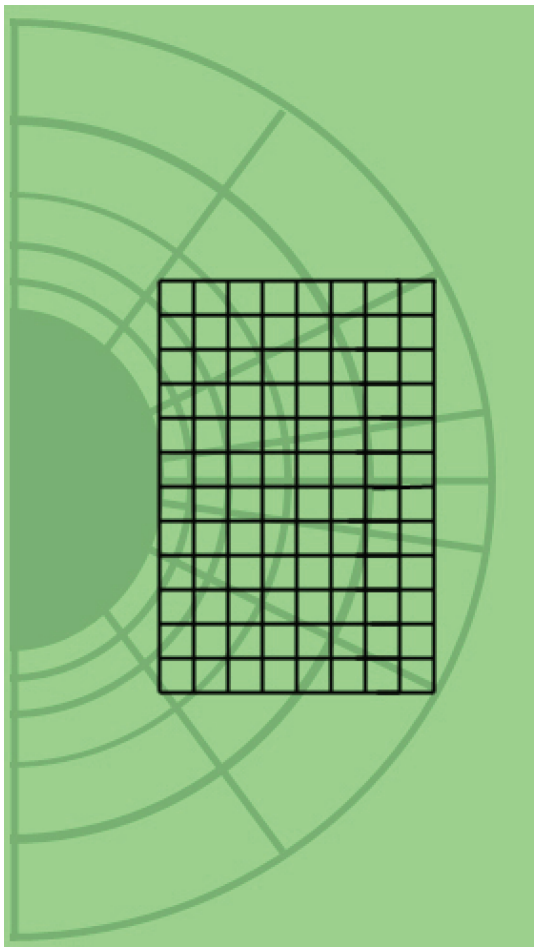

Figure 6. An exaggerated representation of the HARM and MC code grid overlays. The spherically spaced grid underneath is that of the HARM code. The rectangularly spaced grid overlaid is that of the MC code. Both grids are axially symmetric, with said axis on the left-hand side in this image.

or solid, depending on whether the inner radius is set to zero) cylindrical shape. Each zone is assigned a density, ion and electron temperatures, magnetic field amplitude, and thermal and non-thermal distribution components. For our purposes, this is simply set to be a Maxwellian, but the code allows power-law non-thermal distributions as well. The code allows emission from the volume and boundaries, and emitted photons are tracked and allowed to scatter or absorb.

This approach should be quite consistent, but it should be mentioned that the MC code does not include general relativistic (GR) effects. Close to the horizon, the photons' paths should be bent by the high gravity – but this code does not include this effect. However, as was shown in the previous section, densities, temperatures and emissivities are quite low, relatively, near the horizon. Because of this, it is expected that these GR curvature effects would be minimally important for computing the global spectrum.

2.2.1 Coupling GRMHD output to MC input

In Fig. 6, an overlay of the grids for the two codes is shown. It can be easily seen that regardless of how our MC grid is set up, it will almost invariably undersample and oversample the HARM grid at different locations. This is minimized as much as possible by

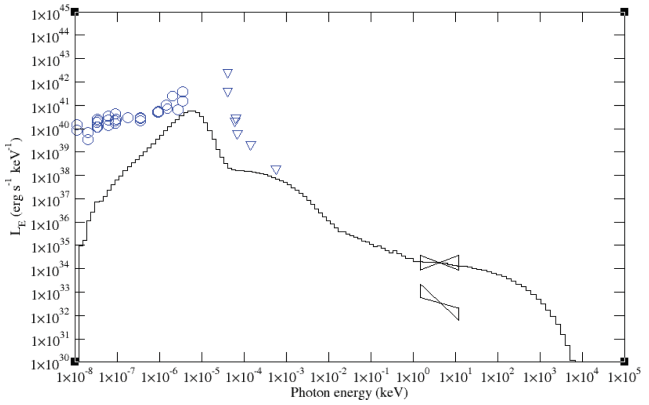

Figure 7. Fit to flaring data with bremsstrahlung component. Maximum values of the 95 × 95 cell grid are scaled to $n = 4.3 \times 10^9$ articles cm^{-3}, $T = 1.2 \times 10^3$ keV, $B = 9.9 \times 10^2$ G. Total luminosity is 3.4×10^{36} erg s^{-1}.

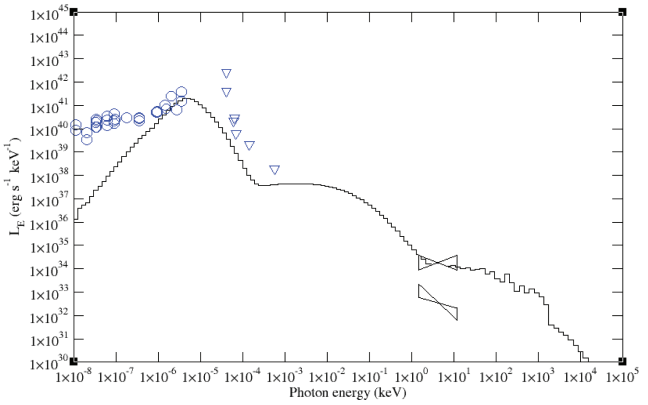

Figure 8. Fit to flaring data with second Compton bump component. Maximum values of the 95 × 95 cell grid are scaled to $n = 3.4 \times 10^8$ articles cm^{-3}, $T = 8.2 \times 10^3$ keV, $B = 1.6 \times 10^2$ G. Total luminosity is 7.5×10^{36} erg s^{-1}.

making a very large MC grid – in our trials, we use a 95 × 95 vertical by radial grid. The grid can actually be quite a bit coarser than this before one notes a significant deviation in the spectrum. As we cannot cover the entire region with a rectangular grid, we have chosen a box which is 28 GM/c^2 radially and 56 GM/c^2 vertically. This box is oriented so that its inner edge is at the horizon.

As noted previously, the output from HARM is completely scalable by black hole mass. For our trials, a rather well-accepted value of 3.6×10^6 solar masses was assigned. We also have the freedom to choose maximum initial density and have the other parameters scale with the density consistently. Density is scalable in this way, since it only reflects a change in accretion rate.

In the HARM output, to determine temperature, we use internal energy. As almost all contributions to this come from ions, we can determine an ion temperature in each zone, but not an electron temperature. The Coulomb coupling is very low due to the low densities expected in the accretion disc of Sgr A* (about 10^6 to 10^{10} articles cm^{-3}), and as the non-thermal heating and cooling mechanisms are not well understood, maximum electron temperature is kept as a free parameter for spectral fitting purposes in this paper. This means that, in effect, we are setting a constant global ratio between T_i, the temperature of the ions, and T_e, the temperature of the electrons, and therefore assuming a two-temperature flow, though this ratio is allowed to change between trials.

We consider the magnetic field given by the HARM data to be the MRI saturated field. As mentioned previously, had we input an initial toroidal field, this would have contributed to the final total field. For this reason, we use the MRI-saturated field as a lower limit to our field value and allow scaling above this.

So, in effect, we set a maximum density, which in turn sets an ion temperature and lower limit to the magnetic field. The electron temperature is freely changed by changing the ratio between T_i and T_e, and the magnetic field can be scaled up from its initial value as necessary.

2.2.2 *Trial and fitting procedure*

Figs 7–11 show observational data points for Sgr A*, whose distance is taken to be approximately 8 kpc, and trial fits. Circles shown represent data points, upside-down triangles are upper limit values and the bowties are flaring and quiescent points from *Chandra* observations presented by Baganoff et al. (2001).

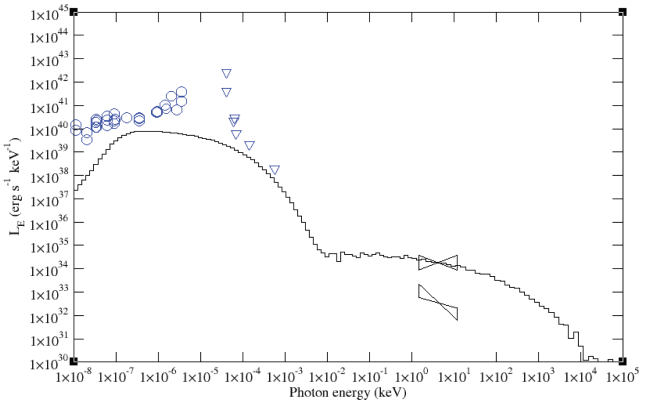

Figure 9. Fit to flaring data with first Compton bump component. Maximum values of the 95 × 95 cell grid are scaled to $n = 5.2 \times 10^6$ articles cm^{-3}, $T = 1.8 \times 10^5$ keV, $B = 13$ G. Total luminosity is 2.6×10^{36} erg s^{-1}.

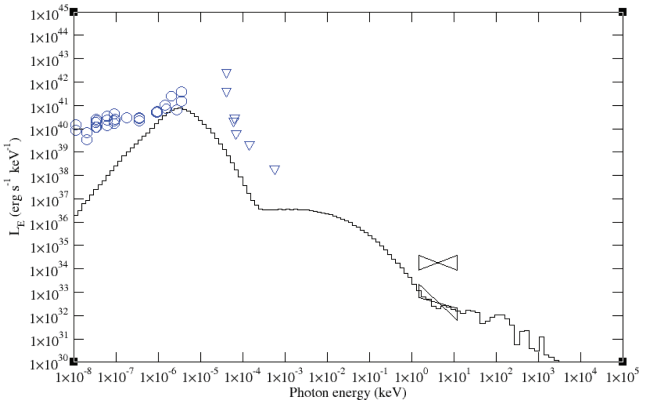

Figure 10. Fit to quiescent data with second Compton bump component. Maximum values of the 95 × 95 cell grid are scaled to $n = 6.9 \times 10^7$ articles cm^{-3}, $T = 8.2 \times 10^3$ keV, $B = 1.6 \times 10^2$ G. Total luminosity is 8.2×10^{35} erg s^{-1}.

Data in the radio to IR range are fairly easy to fit on their own. This is typically done with synchrotron emission arising from the acceleration of moving charges by a magnetic field. When sufficiently energetic, these charges (electrons, in our case) produce a continuum spectrum whose flux and turnover frequency are

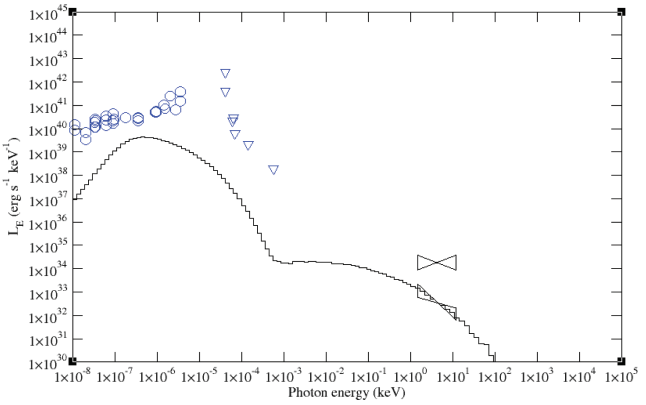

Figure 11. Fit to quiescent data with first Compton bump component. Maximum values of the 95 × 95 cell grid are scaled to $n = 5.2 \times 10^6$ articles cm^{-3}, $T = 4.7 \times 10^4$ keV, $B = 13$ G. Total luminosity is 3.4×10^{34} erg s^{-1}.

directly related to the values of electron temperature, magnetic field and density in this region.

In such a hot medium, synchrotron self-absorption becomes important. This phenomenon occurs when a photon interacts with a charged particle in a magnetic field and transfers its energy to the particle. The low-energy positive slope of the synchrotron curve in each of the trials shown below is due to synchrotron self-absorption.

The difficulties arise in fitting the flaring or quiescent points in the X-ray simultaneously with the radio/IR data. The approach made in this paper is to initially try to fit the flaring point. Its flat slope in L_E suggests that it might be fit by several possible components of the spectrum.

(i) Bremsstrahlung emission, or free–free emission, arises (usually, and in this case) from the acceleration of a free electron by a free nucleus, in a completely ionized plasma. This creates a relatively flat spectrum in L_E out to a cut-off point which corresponds with the temperature of the plasma. The flux of this component is directly related to the square of the density, as it depends on the population of electrons and ions, and also to the square root of the temperature. Temperature also serves to locate the high-energy cut-off in the spectrum. Magnetic field values do not affect bremsstrahlung emission.

(ii) Compton scattering is produced when photons interact with particles (in this case, electrons), leading to changes in energy for both photon and particle. Of interest for our work is inverse-Compton scattering, where a less energetic photon gains energy in an interaction with a hot electron. In general, this tends to form a photon population whose shape is related to the initial photon distribution and the electron distribution it scatters from. This spectrum is typically shifted up in energy an amount approximately equal to the square of the Lorentz factor of the electron population, and drops in flux by an amount equal to the optical depth of the scattering medium. For our trials, the Compton spectrum of importance is mostly generated via synchrotron self-Comptonization (SSC), which refers to the Comptonization of a photon spectrum produced via synchrotron emission by the population of electrons responsible for emitting it to begin with. As the final spectrum resembles the electron distribution and initial (unscattered) synchrotron spectrum, it is possible to locate this spectrum so its flat top intersects the flat flaring X-ray point.

(iii) The second Compton scattering component, as its name suggests, is the spectral component created by the Compton scattering of an already scattered photon population. In this case, it shares the characteristics of the first scattered spectrum, and therefore is a viable component to fit the flaring X-ray point.

All information on emission processes can be found in Rybicki & Lightman (1979).

A large number of MC runs were done to find several sets of parameters which fit this point while remaining consistent with the order of magnitude estimate for total luminosity of 10^{36} erg s^{-1} suggested by Yuan (2007).

The second step in fitting was to attempt to fit the quiescent X-ray data point by varying parameters from those found to fit the flaring point. This was done, specifically, by using the same input values as the flaring point, but by dropping either the density or temperature until the spectrum went through the quiescent point. Depending on the component being fit to the X-ray data, one or both of these parameters could be changed to lower the luminosity to intersect the quiescent point. As we have data showing the variability of mass accretion by HARM, we can estimate reasonable changes in density. Due to the unknown nature of electron heating, it is not inconsistent to suggest that flaring and quiescent points may also arise due to brief moments of higher or lower heating, caused by dissipation of large current sheets in the MRI-turbulence cascade.

It should be noted that observations show a strong correlation between X-ray and radio/IR flux during flares. As it is generally accepted that the lower energy spectral component is due to synchrotron, this lends strength to the idea that the X-ray data are of synchrotron origin – either as a self-Comptonization component or as an extended synchrotron component (Liu & Melia 2001; Markoff et al. 2001; Dodds-Eden et al. 2009).

3 RESULTS

The results presented are shown first for fits to the flaring data (the higher X-ray point), then for fits to the quiescent data (the lower X-ray point). The HARM data used in the MC runs are based on the output at the last time-step ($t = 8000$). Fits are described by the component used to fit the X-ray data. However, this does not indicate that other spectral components were turned off during these runs. For instance, the bremsstrahlung spectrum can be seen to have both first and second Compton bumps, but the spectrum at the X-ray point is almost purely bremsstrahlung.

3.1 Flaring results

Fig. 7 shows an attempt to fit the flaring data with the spectrum's bremsstrahlung component. This is similar to fits attempted by Ohsuga et al. (2005). Like their trials, we have found that the bremsstralung component is too high when the radio data are fit well by the synchrotron data. In this case, we have a simulation volume which extends to 28 GM/c^2, while Ohsuga et al. (2005) have volumes which extend to either 10 or 30R_S (20 or 60 GM/c^2, respectively). They found adequate fits with the smaller volume with a density maximum of 1×10^{10} articles cm^{-3} and with the larger volume at 3.4×10^8 articles cm^{-3}. As would be expected, our trial lies somewhere between the two. However, it seems unlikely that any skewing of density or temperature will allow a fit to the slope of the quiescent data.

Fig. 8 shows a fit by lowering density from the bremsstrahlung fit, but compensating by increasing temperature until the flat portion of the twice-scattered Compton bump fits the slope at the flaring point. Total luminosity and the spectral slope at the flaring point suggest that this is a good fit – and the shape of the spectrum seems

to allude to a possible fit to the quiescent point's slope if density is allowed to drop. As with the bremsstrahlung fit, we can compare the density maximum used in this trial to those of Ohsuga et al. (2005). The value here correlates to that group's lower density and higher volume value – this is reasonable, as we have a significantly higher temperature now.

Fig. 9 shows a fit with low density and high temperature, so the first Compton bump fits the flaring X-ray data point. The synchrotron/synchrotron self-Compton approach was used analytically by Liu et al. (2006), which, while a one-zone approximation, found very similar values to our maximums for one of their trials: $n = 2.3 \times 10^7$ articles cm^{-3}, $T = 1.1 \times 10^5$ keV, $B = 10.2$ G. This fit, like the one above, is promising due to its shape. By lowering only temperature from this value, it appears that the quiescent point may be fit with a similar slope.

3.2 Quiescent results

As alluded to above, quiescent fits for the bremsstrahlung trial, second Compton trial by varying the temperature and first Compton trial by varying the density could be found which intersect the point. However, all of these had nearly zero slopes in $L_{\rm E}$, and were therefore unsatisfactory. We present the two quiescent fits which appeared most promising.

Fig. 10 shows a quiescent fit using the second Compton trial shown in Fig. 8. It should be noted, first of all, that the choppiness in this spectrum is due to the lack of statistics in the twice-scattered photons. Optical depth directly along the equator in this case is approximately 1×10^{-3}, leading to a very small population of scattered photons. The slope at the quiescent point is significantly steeper than the previous trial at the flaring point, and fits the slope required at quiescence well. In this case, we have dropped the density by less than a factor of 5. This is slightly higher than the accretion variation of HARM data, a factor of 2, but is not extreme. As noted in the variation analysis, variations in the density of accreted matter are not considered by HARM, and therefore, changes of this level are not precluded. The results shown here can be changed greatly by small changes in the input values, due to the combination of spectral components required to produce this spectrum.

Fig. 11 shows the quiescent fit for the first Compton trial shown in Fig. 8. This fit was obtained by dropping the temperature by about half an order of magnitude. As noted before, without better understanding of acceleration mechanisms, it is difficult to say whether global temperature changes of this scale are feasible or not. However, by this trial, this approach looks promising, and is closely in line with the idea that correlated low- and high-energy flares arise due to synchrotron radiation – in this case, the X-ray being fit by an SSC component. This trial gives our best fit to the quiescent data point's slope.

4 CONCLUSIONS

We have presented results for coupled physical and spectral simulations of the accretion disc of Sgr A*. Fits to flaring X-ray data are shown for three sets of parameters of an entirely thermal plasma, and these results are discussed, noting their similarities to two other recent models made for this same situation. The values used in our trials for all three sets of parameters are quite similar (respectively) to those used by Liu et al. (2006) and Ohsuga et al. (2005).

Of these, the trials which fit the flaring data point with the first Compton bump and second Compton bump show promise to allow fits to the quiescent X-ray data by only changing one physical value. The second Compton bump trial shows a promising fit which intersects the quiescent point by dropping the density, and may be at an appropriate slope. This trial is also the best fit to low-energy data while fit to the X-ray points. While intersecting each X-ray point, some of the IR data are fit by the synchrotron bump. The first Compton bump trial shows a very good fit, in both slope and position, to the quiescent point by dropping the temperature, though these trials never match the IR or radio data points. The second Compton bump fit appears approximately valid in comparison to the variations in mass accretion on to the black hole suggested by the HARM output. It should be noted, as reported in Xu et al. (2006), the quiescent state X-ray emission can be attributed to thermal emission from the large-scale accretion flow. For this reason, the data point we have fit here could be considered an upper limit.

Overall, we present our second Compton bump trials as our best explanation for the observed spectra of Sgr A*. Due to the combination of spectral components at the critical point in the X-ray, we are able to describe a large number of different slopes and locations – with these being quite sensitive to input values. This may account for the observed variability in X-ray slopes and luminosities.

While our second Compton trial can fit the IR points, it is found that none of our fits can match the radio data well while also fitting X-ray data – this suggests that a completely thermal approach using GRMHD and one-temperature electrons is lacking in ways that may be improved by using FP techniques or results suggested by recent kinetic simulations of turbulence-heated electron distributions (Liang 2009). It is also possible that a larger simulation volume must be enclosed to fit these points concurrently with the X-ray data.

In the future, this project will turn to some method of consistently introducing non-thermal particle acceleration to determine whether this can provide better fits to the joint radio/IR/X-ray data.

ACKNOWLEDGMENTS

This work was supported by a Los Alamos National Laboratory IGPP research grant and NSF-AST-0406882.

The authors would like to thank a number of people whose input helped shape this work, including, but not limited to, Markus Böttcher, Xuhui Chen, Justin Finke, Charles Gammie and Feng Yuan.

REFERENCES

Abramowicz M. A., Chen X., Kato S., Lasota J.-P., Regev O., 1995, ApJ, 438, L37
Baganoff F. K. et al., 2001, Nat, 413, 45
Baganoff F. K. et al., 2003, ApJ, 591, 891
Balbus S. A., 2003, ARA&A, 41, 555
Balick B., Brown R., 1974, ApJ, 194, 265
Bélanger G., Goldwurm A., Melia F., Ferrando P., Grosso N., Porquet N., Warwick R., Yusef-Zadeh F., 2005, ApJ, 635, 1095
Böttcher M., Liang E. P., 1998, ApJ, 506, 281
Böttcher M., Liang E. P., 2001, ApJ, 552, 248
Böttcher M., Liang E. P., Smith I. A., 1998, A&A, 339, 87
Böttcher M., Jackson D. R., Liang E. P., 2003, ApJ, 586, 339
Canfield E., Howard W. M., Liang E. P., 1987, ApJ, 323, 565
Dodds-Eden K. et al., 2009, ApJ, 698, 676
Eckart A. et al., 2004, A&A, 427, 1
Eckart A. et al., 2006, A&A, 450, 535
Finke J., 2007, PhD thesis, Ohio Univ.
Finke J. D., Bottcher M., 2005, PASP, 117, 483
Fishbone L. G., Moncrief V., 1976, ApJ, 207, 962

Gammie C. F., McKinney J. C., Toth G., 2003, ApJ, 589, 444
Ghez A. M. et al., 2003, ApJ, 586, L127
Goldston J. E., Quataert E., Igumenshchev I. V., 2005, ApJ, 621, 785
Hawley J. F., 2001, ApJ, 554, 534
Hawley J. F., Balbus S. A., 2002, ApJ, 573, 738
Ichimaru S., 1977, ApJ, 214, 840
Igumenshchev I. V., Narayan R., Abramowicz M. A., 2003, ApJ, 592, 1042
Kato Y., Mineshige S., Shibata K., 2004, ApJ, 605, 307
Liang E., 2009, preprint (arXiv:0902.4740)
Liang E. P., Dermer C. D., 1988, ApJ, 325, L39
Liu S., Melia F., 2001, ApJ, 561, L77
Liu S., Petrosian V., Melia F., Fryer C. L., 2006, ApJ, 648, 1020
Markoff S., Falcke H., Yuan F., Biermann P. L., 2001, 379, L13
Martin K. W., Liu S., Fragile C., Yu C., Fryer C. L., 2009, preprint (arXiv:0904.0118)
Melia F., 2006, The Galactic Supermassive Black Hole. Princeton Univ. Press, Princeton, NJ
Narayan R., Yi I., 1994, ApJ, 428, L13
Narayan R., Yi I., Mahadevan R., 1995, Nat, 374, 623
Noble S. C., Gammie C. F., McKinney J. C., Del Zanna L., 2006, ApJ, 641, 626
Ohsuga K., Kato Y., Mineshige S., 2005, ApJ, 627, 782
Rybicki G. B., Lightman A. P., 1979, Radiative Processes in Astrophysics. Wiley, New York
Schödel R. et al., 2002, Nat, 419, 694
Shakura N. I., Sunyaev R. A., 1973, A&A, 24, 337
Xu Y. et al., 2006, ApJ, 640, 319
Yuan F., 2007, ASP Conf. Ser. Vol. 373, p. 95
Yuan F., Quataert E., Narayan R., 2003, ApJ, 598, 301

This paper has been typeset from a TEX/LATEX file prepared by the author.

The Astrophysical Journal, 746:87 (11pp), 2012 February 10 doi:10.1088/0004-637X/746/1/87

NUMERICAL MODELING OF MULTI-WAVELENGTH SPECTRA OF M87 CORE EMISSION

G. Hilburn and E. P. Liang
Physics and Astronomy Department, Rice University, Houston, TX 77005, USA; guy.l.hilburn@rice.edu
Received 2011 September 13; accepted 2011 December 16; published 2012 January 27

ABSTRACT

Spectral fits to M87 core data from radio to hard X-ray are generated via a specially selected software suite, comprised of the High-Accuracy Relativistic Magnetohydrodynamics GRMHD accretion disk model and a two-dimensional Monte Carlo radiation transport code. By determining appropriate parameter changes necessary to fit X-ray-quiescent and flaring behavior of M87's core, we assess the reasonableness of various flaring mechanisms. This shows that an accretion disk model of M87's core out to 28 GM/c^2 can describe the inner emissions. High spin rates show GRMHD-driven polar outflow generation, without citing an external jet model. Our results favor accretion rate changes as the dominant mechanism of X-ray flux and index changes, with variations in density of approximately 20% necessary to scale between the average X-ray spectrum and flaring or quiescent spectra. The best-fit parameters are black hole spin $a/M > 0.8$ and maximum accretion flow density $n \leqslant 3 \times 10^7$ cm^{-3}, equivalent to horizon accretion rates between $\dot{m} = \dot{M}/\dot{M}_{\rm Edd} \approx 2 \times 10^{-6}$ and 1×10^{-5} (with $\dot{M}_{\rm Edd}$ defined assuming a radiative efficiency $\eta = 0.1$). These results demonstrate that the immediate surroundings of M87's core are appropriate to explain observed X-ray variability.

Key words: galaxies: active – galaxies: nuclei – X-rays: individual (M87)

Online-only material: color figures

1. INTRODUCTION

It is generally accepted that the center of the Faranoff–Riley type I (FR-I) radio galaxy M87 harbors a supermassive black hole of mass $(6 \pm 0.5) \times 10^9 M_o$ (Gebhardt & Thomas 2009) at a distance of 16.7 Mpc (Mei et al. 2007), which is associated with a spectacular kiloparsec scale jet. Observations of superluminal motion in the jet require a jet viewing angle of $\theta < 19^\circ$ and bulk Lorentz factor $\gamma > 6$ at the prominent HST-1 jet knot, which would imply that it is located $5.3 \times 10^5 R_s$ downstream from the core (Biretta et al. 1999; Cheung 2007), where the Schwarzschild radius of the black hole $R_s = 1.8 \times 10^{15}$ cm (Hardee 2010). Due to its size, proximity, and orientation, M87 provides a unique opportunity for study of a central active galactic nucleus (AGN) environment, which can be probed to investigate particle energization in accretion disks, jet launching, and other astrophysical phenomena occurring in these extreme situations.

Its spectral energy distribution (SED) suggests that M87 is a misaligned BL Lac object. It has been observed for a number of years from radio to gamma rays, and detailed information is available from multi-wavelength collaborations (Acciari et al. 2008, 2010). M87's core is variable, and optical and X-ray bands show common changes of about a factor of two, on timescales of months (Perlman et al. 2003; Harris et al. 2009). Very high energy (VHE) observations of variability on timescales of days (Aharonian et al. 2006) suggest very compact emission regions on the order of the size of the inner accretion disk (Neronov & Aharonian 2007), and concurrent VHE, radio, and X-ray campaigns have helped tie the gamma-ray emission from M87, for specific events, to areas close to the core (Abdo et al. 2009).

A number of models have been proposed in recent decades to describe accretion disks in AGN systems with low luminosity, compared to their Eddington luminosity (the luminosity limit at which the radiative pressure on the accreting matter balances the gravitational pull by the center body)—an idea which has been referred to as a radiatively inefficient accretion flow (RIAF; Yuan et al. 2003). Popular among these is the advection-dominated accretion flow (ADAF) model, which cites the idea that, close to the horizon, most of the gravitational energy gained by particles is unable to radiate prior to them being advected onto the black hole (Narayan & Yi 1994). The luminosity of M87 is about $L \approx 10^{-6} L_{\rm Edd}$, where Edd represents the Eddington luminosity. di Matteo et al. (2003) suggest an upper limit to the accretion rate of M87 around $\dot{m} = \dot{M}/\dot{M}_{\rm Edd} = 1.6 \times 10^{-3}$, the Bondi accretion rate, based on gas properties derived from the Compton spectrum, where $\dot{M}_{\rm Edd}$ is the accretion rate at which the Eddington luminosity is reached, assuming a radiative efficiency $\eta = 0.1$, representing the fraction of energy radiated by a typical particle of its total energy. This would suggest that the efficiency of the source is $\eta \approx 10^{-5}$ if it accretes at $\dot{M}_{\rm Edd}$, much lower than the canonical value $\eta = 0.1$ in a standard, efficient thin disk, making it a truly radiatively inefficient source. A more recent estimate by Levinson & Rieger (2011) based on calculated jet power and the capability of the system to extract power from a Kerr black hole suggest an accretion rate $\dot{m} = 10^{-4}$, for a maximally rotating black hole ($a/M = 1$). Smaller spin values would then suggest higher accretion rates, scaling as $\dot{m}$ proportional to a^{-2}. These rates may or may not be calculated at the black hole horizon, as some models choose other radii. These accretion rate estimates can help set particle densities in radiative models.

Models based on specific radiative mechanisms have been invoked recently to describe M87's spectrum. For instance, Neronov & Aharonian (2007) suggest a scheme where electrons are accelerated by vacuum gap electric fields, in the black hole magnetosphere, while another paper makes use of centrifugal acceleration to heat electrons which upscatter ADAF disk photons (Rieger & Aharonian 2008). Models such as these which propose novel acceleration methods are generally seeking to explain the heating of electrons to VHEs, which then, through the inverse Compton process, upscatter synchrotron photons to complete the X-ray and VHE spectrum (Hardee 2010).

Recent modeling work has attempted to restrict possible spin rates for M87 via a number of methods. These papers typically use the rapid TeV variability to probe the black hole angular

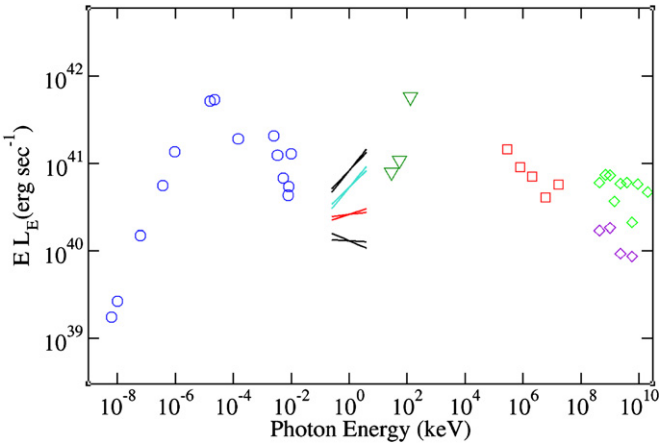

Figure 1. SED of M87 in EL_E, to depict the variety of *Chandra* X-ray indices. Inverted triangles are *Swift* long-term monitoring upper limits. They will only be used to restrict fits to the average *Chandra* spectrum (shown as the red bowtie), as flares are short-term transients.

(A color version of this figure is available in the online journal.)

momentum, as in Wang et al. (2008), where the TeV optical depth, assuming ADAF, is shown to strongly depend on the spin and constrains it to greater than $a/M = 0.65$. Similarly, the same group, in Li et al. (2009), solves the relativistic hydrodynamical equations in the RIAF scheme to constrain the spin to greater than $a/M = 0.8$. Advanced TeV imaging is likely to provide a very useful tool to tie down black hole spins in the near future. For this paper, the lower limit on spin for M87 is assumed to be $a/M = 0.65$, to evaluate how well different spin rates fit the observed SED.

We consider a scenario in which the immediate surroundings of the central black hole are responsible for the radio, infrared, and X-ray emissions observed. This is due to emitting electron populations within the accretion flow and any general relativistic magnetohydrodynamic (GRMHD)-driven outflows which High-Accuracy Relativistic Magnetohydrodynamics (HARM) develops consistently. Moreover, this region may prove to be the origin of VHE emission, though due to the VHE electrons necessary to produce these through inverse Compton scattering, and the very low photon counts, this is a very difficult part of the spectrum to simulate via Monte Carlo (MC) methods. Unlike other recent models focused on the radio–IR emissions, in this paper, we do not attempt to explain the energization method of electrons. Rather, we assume electron temperatures to be a free parameter proportional to the ion temperature due to the compressional heating inherent in MHD accretion methods. The focus for this paper is on the dynamics specific to spin and accretion rates which produce appropriate Compton spectra. This constant electron-to-ion temperature ratio is a common assumption (Goldston et al. 2005; Moscibrodzka et al. 2009), as there is no consensus on particle heating, and only work which is specifically related to heating mechanisms, such as Shcherbakov & Baganoff (2010), shows evidence against this.

To motivate this constant temperature ratio assumption, recent particle-in-cell (PIC) simulations (Zenitani & Hoshino 2005, 2007; Liang 2009; Liu et al. 2011) demonstrated that magnetic reconnection and current sheet dissipation, which are believed to be the dominant kinetic processes dissipating magnetorotational instability (MRI)-driven turbulence, efficiently convert magnetic energy into hot electron thermal energy even in the absence of collisions. Since the saturated MRI magnetic pressure given by MHD simulations scales with ion pressure, it is reasonable to expect the electron pressure heated by collisionless processes to scale with ion pressure. Hence, as discussed above, for our models the electron temperature scales with ion temperature.

Table 1
Table of *Chandra* X-Ray Spectra

Label	Date	Flux (10^{40} erg s^{-1})	Spectral Index[a]
Flare1	2008 Feb 16	8.24 ± 0.13	0.62 ± 0.031
Flare2	2008 Jun 24	5.29 ± 0.11	0.64 ± 0.035
Average	...	2.59 ± 0.055	0.92 ± 0.044
Quiescent	2007 Jul 31	1.31 ± 0.047	1.08 ± 0.062

Notes. *Chandra* data are taken from the 0.2 to 6 keV band.
[a] Index α for a power-law fit: $F_\nu \propto \nu^{-\alpha}$.

This paper will focus on fitting data in the radio, IR, optical, and X-ray regimes (Section 2), particularly the *Chandra*-band X-ray variability, of the SEDs by calculating physical properties via a GRMHD accretion disk evolution scheme (Section 3.1) and applying output to a specialized MC radiation transport code (Section 3.2) by our specific modeling method (Section 4). Section 5 and Section 6 will contain interpretations of the data presented, detailing ramifications of results for clarifying the picture of M87's nucleus. Suggestions regarding likely spin rate, accretion rate, and the mechanism of flaring will be presented, and reasonable modeling tasks for the future, based on the results, will be discussed. Finally, the Appendix details modifications to the MC code for these types of sources, with highly anisotropic magnetic and velocity fields.

2. OBSERVATIONS

M87 has been extensively observed throughout its energy range for decades. Collected here is a full spectrum of data to describe its emissions, all plotted in Figure 1. In the radio regime, data are available from the *IRAM* Plateau de Bure interferometer (Despringre et al. 1996) and the NRAO/Very Large Array (Biretta et al. 1991). At slightly higher energies, in IR, data are shown from Gemini Observatory/OSCIR (Perlman et al. 2001), the Subaru Observatory/COMICS, and *Spitzer Space Telescope*/Infrared Spectrograph/MIPS/Infrared Array Camera (Perlman et al. 2007). Next, in optical, Biretta et al. (1991) presented data from the *Palomar* telescope. These lower energy data are all represented as open circles in Figure 1.

In hard X-ray, *Swift*/BAT has provided upper limits from observations from 2005 to 2009 (Ajello et al. 2008, 2009) which are shown as inverted triangles in Figure 1. Observations in VHE have also been collected, by HEGRA (Aharonian et al. 2003, 2004), H.E.S.S. (Aharonian et al. 2006), and *Fermi*-LAT (Abdo et al. 2009), with flaring behavior shown from H.E.S.S. LAT data are shown as squares while H.E.S.S. flaring and quiescent data are depicted as diamonds.

The most important data collected are from the *Chandra* X-ray telescope, which are shown in Figure 1 as bowties. Results were first given by Wilson & Yang (2002), and variability data and descriptions of the observations and data used here are presented in Harris et al. (2009). D. Harris & F. Massaro (2011, private communication) and their group yielded spectral details which allowed for consideration of a variety of quiescent and flaring X-ray spectra. Shown in Figure 1 and Table 1 are two flaring *Chandra* X-ray spectra, a quiescent spectrum, and an average spectrum obtained by averaging the flux and power-law

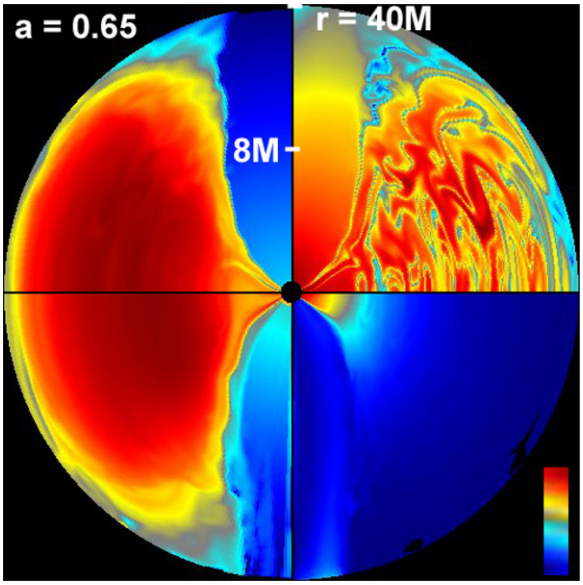

Figure 2. Composite image of HARM output, showing data from runs with black hole spin $a/M = 0.65$, at time $t = 2000\,M$. The top and bottom on the left show density and internal energy (temperature × density) plots, respectively. The top and bottom on the right are magnetic field squared and bulk Lorentz factor, respectively. Dark red corresponds to the highest normalized value for each, dark blue to the lowest. Included are marks to depict the radial logarithmic spacing.

(A color version of this figure is available in the online journal.)

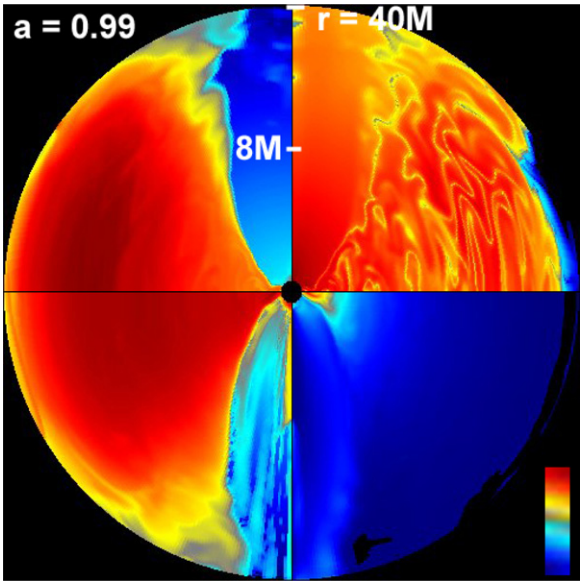

Figure 3. Composite image of HARM output, as above, for a run of $a/M = 0.99$, at time $t = 2000\,M$. Important to note is the dramatically stronger polar outflows, particularly visible in the internal energy (lower left) plot. Only the higher spin runs show considerable emission contributions from this region.

(A color version of this figure is available in the online journal.)

spectral index (α for $F_\nu \propto \nu^{-\alpha}$) of all *Chandra* data. The highest flaring spectrum is significantly greater in flux than any other data point, so this paper will focus on fitting the second flaring point, which is more in line with the general trend of data. So, any mention of the flaring *Chandra* X-ray spectrum from this point on will refer to the second highest flaring point (Flare2 in Table 1). The Flare1 bowtie will be left out of any further figures.

3. SIMULATION TOOLS

3.1. HARM GRMHD Code

The physical values of the accretion disk system are calculated with the two-dimensional (2D) axisymmetric HARM GRMHD code, which evolves an accreting black hole system based on a number of simple user-adjustable parameters as described in Gammie et al. (2003) and Noble et al. (2006). From an initial torus perturbed from equilibrium by a small poloidal magnetic field, HARM integrates the GRMHD equations in a conservative scheme to consistently calculate parameters of the accretion flow. Conserved variables are tracked by evaluating fluxes between simulation cells, and, from these, primitive physical variables such as particle density, internal energy, magnetic field, and velocity are calculated (see Figures 2 and 3). For a full description of HARM'S algorithms and method, please see the cited papers (Gammie et al. 2003; Noble et al. 2006).

For our purposes, HARM is set up with a small number of user-defined parameters, including adiabatic index, black hole spin value, simulation box size, torus position, and a small poloidal magnetic field to seed the torus. From these initial parameters, the accretion disk evolves, governed largely by the MRI, which describes the outward transport of angular momentum in the disk, and generates turbulence in the magnetic field from an initially poloidal field. The physical space is

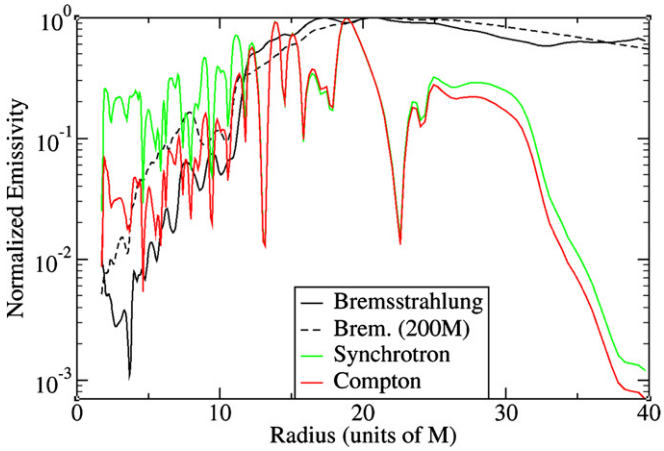

Figure 4. Normalized emissivities for a typical $a/M = 0.65$ run. Shown for comparison as the dashed line is a bremsstrahlung emissivity curve from an HARM run encompassing a volume out to $r = 200\,M$. The curve labeled "Compton" is the generalized Compton emissivity, the synchrotron emissivity multiplied by the electron density.

(A color version of this figure is available in the online journal.)

divided into a spherical radial/angular grid, with cells spaced logarithmically in radius, and concentrated equatorially in the angular dimension. This gives the highest resolution along the equator, at the horizon, where the shortest length scales of importance are located.

In order to construct a useful library of LLAGN results from HARM, we have made a number of overlapping runs, all with an adiabatic index of 5/3, on grids of resolution 256 × 256 and 512 × 512. These runs span a range of black hole spin value $a/M = 0.65$, 0.8, 0.9, and 0.99, the last being a near-maximally rotating black hole. To check the effect of including larger simulation volumes, we have also made runs whose outer radii (in GM/c^2) range from 40 to 200. Multiple simulation volumes can also be used to test for convergence of results given by the radiation transport code, given different volumes enclosed. Emissivity curves are shown in Figure 4, to give an idea of the location

of peak emission for different radiative mechanisms. Important to note is that the bremsstrahlung curve peaks within $r = 22\,M$, whether larger volumes are considered or not, so most of the region's emissions will be reasonably modeled by using the smaller, better resolved, volume.

A brief note on the appropriateness of using 2D GRMHD for the problems being investigated: we contend that for our purposes of creating broadband spectra and constraining global parameters, the details of azimuthal modes would be averaged out even if included in full 3D, due to the rapid disk rotation in most of the relevant emission region. That is, the global spectra of a 2D trial should look approximately the same as a 3D trial, given matching parameters. This was noted by Ohsuga et al. (2005) in regard to Sgr A*, who stated that they checked that final MC generated spectra were not significantly changed by averaging 3D MHD parameters over azimuth, implying that 3D effects may not be vital to conduct global spectral studies. A primary difference in 3D and axially symmetric simulations is that MRI turbulence decays due to Cowling's anti-dynamo theorem throughout axially symmetric simulations. Due to this, care is taken to select data at $t = 2000\,M$ (in black hole units) during the optimally turbulent time following initial infall, before the decay phase of the 2D turbulence.

3.2. Monte Carlo Radiation Transport Code

The emission spectra based on physical parameters from HARM simulations are calculated by feeding the GRMHD data into our 2D axisymmetric MC relativistic radiation transport code (Canfield et al. 1987; Liang & Dermer 1988; Boettcher et al. 2001; Finke & Boettcher 2007; Chen et al. 2011). This simulation scheme allows bremsstrahlung and synchrotron emission, based on the radiative weight of each zone. Emissions are then tracked through the simulation volume, with their energies and photon weights adjusted by absorption and scattering.

All MC runs presented are on a 95×95 cell cylindrical grid, evenly spaced radially and vertically, in contrast to the spherical grid used by HARM (Figure 5). The 95×95 grid is much finer than, for instance, 50×50 MC runs which present very similar results. Based on a number of different mesh trials, the data are convergent at this scale. The mapping procedure for physical values, from the HARM grid to the MC code grid, relies on averaging the values for all HARM cells that lie within each (usually much larger) MC code cell. The number of MC photons (each representing a huge number of actual photons, reflecting the actual emission level of the zone) used for each run is 1–10 million. Runs which needed more Compton scattering statistics relied on the photon splitting technique developed by Chen et al. (2011). This significantly increases the quality of scattering statistics, allowing for both more consistent and shorter runs.

This code has the capability to evolve electron distributions based on the Fokker–Planck (FP) equation. Given that the electron-heating mechanism in LLAGN accretion disks is poorly understood and most likely due to collisionless plasma processes, we feel that it is inappropriate to use the FP equation, so it is turned off for all trials. As a first estimate, electrons are assumed to be thermal at a set temperature proportional to ions. Future work will use PIC simulation results on the nonthermal heating of electrons by magnetic turbulence (Liang 2009; Liu et al. 2011).

In order to better model these types of sources, with highly anisotropic magnetic and velocity fields, modifications to the emission and scattering methods of the code were necessary and are detailed in the Appendix.

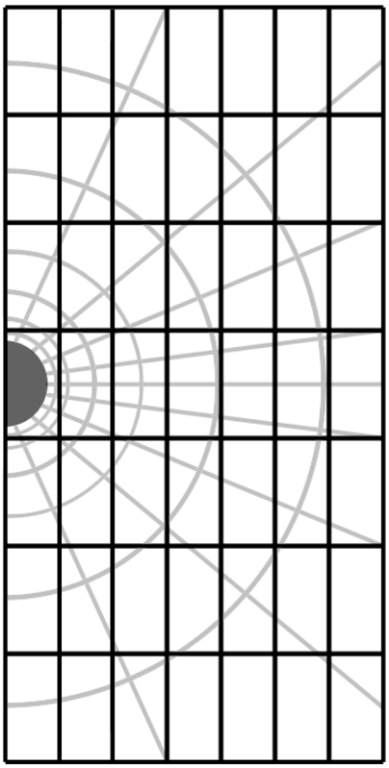

Figure 5. Schematic depiction of the MC code (cylindrical, axisymmetric) grid overlaid on the HARM (spherical, axisymmetric, logarithmic) grid. The HARM grid is much finer than the MC grid close to the horizon (shown as a solid semicircle), and somewhat larger at large radii. In this image, the respective grids are at appropriate ratios to one another through the simulation volume, though the horizon is exaggerated compared to the grid size. In actual simulations, about seven MC cell lengths fit inside a Schwarzschild radius. To model the horizon in the MC code, any cells within its radius are purely absorbing.

4. MODELING

Evaluating HARM output to supply input data to the radiation transport code requires several steps, as described in Hilburn et al. (2010).

1. All HARM units scale with a specified black hole mass, so the same runs may be applied to various astrophysical sources. Specifying the black hole mass and a maximum density for the accretion flow yields values throughout the grid for MRI-saturated magnetic field components, ion temperatures due to adiabatic compressional heating, particle densities, and velocity components.
2. The MRI-saturated magnetic field values output by HARM are considered lower limits, as they do not include additional primordial fields (largely azimuthal) that may have been present in the plasma before its accretion. Despite starting with a purely poloidal field, the azimuthal component of the field dominates due to the MRI evolution. When scaling the magnetic field values for MC input, the amplitude is increased and components retain their respective ratios. Because the azimuthal component is dominant to begin with, this approximation is equivalent to adding a primordial azimuthal field.
3. As the electron-heating mechanism in LLAGN accretion disks is poorly understood, a parameterized globally uniform electron-to-ion temperature ratio is applied, as in

Goldston et al. (2005) and Moscibrodzka et al. (2009). This ratio is ultimately determined by collisionless (anomalous) heating processes, more efficient than Coulomb collisions. This is acknowledged as a first approximation and implies that the level of compressional heating of ions is proportional to the total heating of electrons, likely largely from magnetic dissipation. In the future, for more advanced models, we will add a small nonthermal (power-law) component to the thermal population to model the VHE data.

So, given a black hole mass, maximum density, magnetic field value (over the MRI-saturation value), and electron-to-ion temperature ratio, HARM output can be used to compute radiation output. In this case, the maximum value of each parameter is set, and each other cell's value scales accordingly.

4.1. Spectral Modeling Results

Typical HARM data were taken at $t \approx 2000\,M$, before accretion-driven turbulence dies down. At this point, we used the HARM output as input to the MC spectral modeling. The particle densities chosen for models are based on accretion rates suggested in the literature. When the maximum particle density is $n = 1 \times 10^7$ cm^{-3}, the maximum accretion rate within the simulation volume is $\dot{m}_{\rm max} \approx 10^{-4}$. This is the case for all spin rates, while the accretion rate through the horizon ranges from $\dot{m}_H \approx 2 \times 10^{-6}$ up to $\dot{m}_H \approx 2 \times 10^{-5}$, depending on the specific model—higher spin rates have correspondingly lower horizon accretion rates, due to outflows. As the maximum matches the accretion estimates of recent work, this was chosen as a benchmark for our models. For the rest of the paper, accretion rates will be given as maximum values as these are similar between models with differing spin rates. In order to evaluate the impact of a higher or lower accretion rate, two other maximum densities were chosen: $n = 3 \times 10^6$ cm^{-3} and $n = 3 \times 10^7$ cm^{-3}, for maximum accretion rates of $\dot{m}_{\rm max} \approx 3 \times 10^{-5}$ and $\dot{m}_{\rm max} \approx 3 \times 10^{-4}$, respectively. Full trials were then performed using these three densities, leaving two parameters for adjustment: electron temperature and magnetic field.

As the main interest in fitting spectra is to evaluate the origin of flaring mechanisms, runs are chosen for their fits to X-ray data. The starting point for each density is then to fit the average X-ray spectrum, whose flux and index are averaged over all *Chandra* X-ray data, not including those with possible pileup.

Figure 6 shows the effect of changing each parameter (density, temperature, and magnetic field) by a factor of two. Obviously, temperature and density have a significant impact on the spectral shape at the X-ray spectrum, each hardening the spectrum when raised. Conversely, the magnetic field, in general, uniformly changes the flux throughout the X-ray spectrum, without changing the X-ray spectral index considerably. This is because increasing the magnetic field increases the flux of the synchrotron curve at the same rate it increases that of the Compton components, as the upscattered photons are synchrotron in origin.

As the density in each trial is fixed, this means that the obvious method of fitting spectra is to vary temperature to fit spectral index while varying magnetic field to fit flux, until the average X-ray bowtie is satisfactorily fit. It should be noted that, in general, higher black hole spin rates lead to higher densities at small radii, where velocities of the accreting matter are much greater. Higher velocities lead to harder spectra due to Doppler boosting, so higher spin trials have lower indices, for similar parameters.

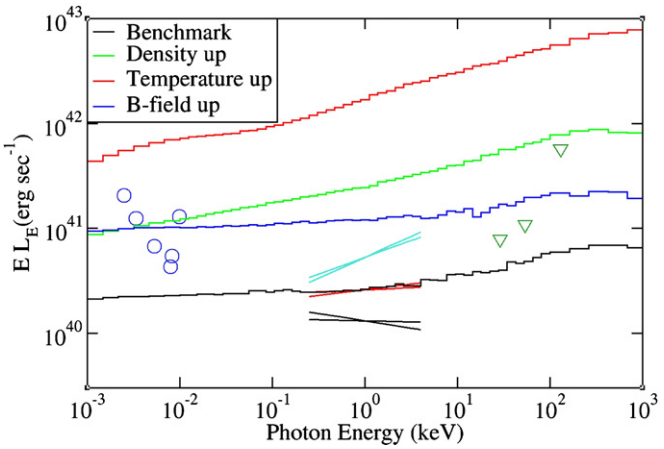

Figure 6. Benchmark fit at $a/M = 0.9$, $n = 1 \times 10^7$ cm^{-3}, and three spectra generated by alternately raising a single parameter by a factor of two. This is shown in EL$_E$, to better depict index changes in X-ray.

(A color version of this figure is available in the online journal.)

Once full trials were completed to fit the average X-ray spectrum—for each of the three density points and for each of the four black hole spins—the quiescent and flaring spectra needed consideration. Given that the flaring mechanism is unknown, the simplest changes to interpret involve varying a single parameter each time. Specifically, if a change in accretion rate is responsible for the flaring behavior, we approximate it by a global density change at fixed temperature. If an increase in electron heating is responsible, we model this by a global temperature change at fixed density. For this reason, a full suite of trials has been done which fit the quiescent and flaring X-ray spectra by changing merely one of these (maximum density, maximum electron temperature) from the benchmark model which fits the average X-ray spectrum.

Since the $n = 1 \times 10^7$ cm^{-3} runs have the closest accretion rate to that suggested in literature ($\dot{m}_{\rm max} = 10^{-4}$) these runs were evaluated first. The fits for each spin rate are normalized to match the flux of the average X-ray spectrum. In general, these are poor fits to radio, IR, and optical data. Because the higher spin rates lead to larger densities at higher accretion velocities, and therefore harder spectra, the $a/M = 0.99$ trial had to use the lowest temperature value, and, conversely, the 0.65 trial the highest, to fit the slope of the X-ray data. This leads to the lower spin rates providing better fits at low energies, as the synchrotron flux is higher. However, none of these adequately fits any of the low-energy spectrum, so the quiescent and flaring fits are not considered.

The fits for the $n = 3 \times 10^6$ cm^{-3} runs, which yield an accretion rate lower than suggested by literature, are qualitatively similar to those discussed above. They fall short at the radio–IR range; therefore, quiescent and flaring trials are again not considered.

4.2. Fits Using a Density of 3×10^7 cm^{-3}

The third set of fits uses a density of $n = 3 \times 10^7$ cm^{-3}. This corresponds to an accretion rate above the recently quoted value, but still well below the Bondi accretion rate which has been suggested as an upper limit to the level of accretion. The Bondi accretion rate defines spherical accretion onto a compact object, $\dot{M} = \pi R^2 \rho v$, where ρ and v are the density and sound speed, respectively, of accreting matter, and R is the characteristic radius found by equating the object's escape velocity and relevant sound speed (di Matteo et al. 2003).

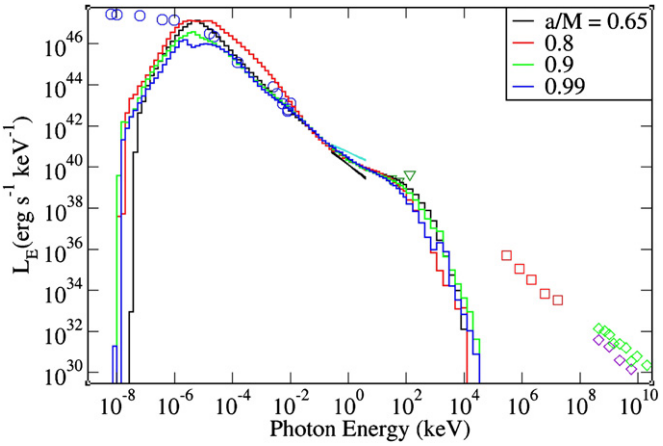

Figure 7. $n = 3 \times 10^7$ cm^{-3} runs. Below are quiescent and flaring fits, as these runs describe lower energy data best.

(A color version of this figure is available in the online journal.)

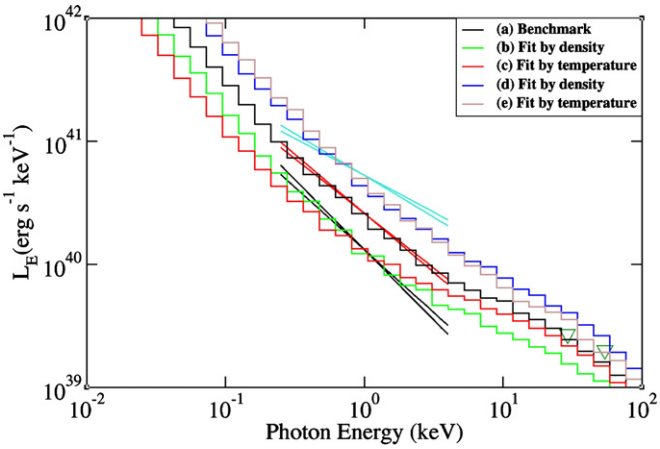

Figure 8. $a/M = 0.9$, with $n = 3 \times 10^7$ cm^{-3}. These views are zoomed in to focus on the X-ray spectra, to better show changes in index here. (a) is the average fit shown above. Fits to quiescent data, (b) and (c) are varied from (a) in density and temperature, respectively. Flaring fits (d) and (e) are varied in density and temperature, respectively. That is, (c) and (e) are changed only in temperature from (a), and similarly for (b) and (d) in density.

(A color version of this figure is available in the online journal.)

As seen in Figure 7, these spectra offer good fits to radio, IR, and optical data, unlike lower density trials. The second big change is the visibility of the shoulder of the bremsstrahlung emission in hard X-ray, above *Chandra* energies. This is the first time here the upper limits from *Swift* data (Ajello et al. 2008, 2009) require consideration. As *Swift* data are averaged limits over several years, they only restrict fits to the average *Chandra* X-ray spectrum, but they are still right at the edge of all the spectra with this density. Essentially, as bremsstrahlung emission scales as density squared, this puts a limit on maximum model density at $n = 3 \times 10^7$ cm^{-3}.

While the $a/M = 0.8$ trial overestimates much of the low-energy data, three of the four fits shown above are approximately equally good through the radio, IR, and optical bands. All also fit with a nearly pure power law at the average X-ray spectrum and come close to the *Swift* X-ray upper limits. The only fit which lies comfortably beneath the *Swift* upper limits is the $a/M = 0.99$ run. This is due again to the fact that with higher spin runs, the emitting/scattering electron populations are moving with higher maximum bulk velocities. This means that the maximum temperature can be turned down considerably while still maintaining the appropriate X-ray index, thereby moving the bremsstrahlung cutoff to a substantially lower energy than the other trials.

The quiescent and flaring fits shown in Figure 8 are for the runs with $a/M = 0.9$. Shown as (a) is the average fit shown in the zoomed out image above (Figure 7). As detailed in the fitting methodology, the quiescent and flaring fits are changed from the average data fit in only one parameter: either temperature or density. Spectra (c) and (e) are changed only in temperature from the benchmark (a), while (b) and (d) are changed only in density.

Either quiescent trial could be seen to fit the quiescent spectrum reasonably; its index is quite similar to the average spectrum. The bremsstrahlung shoulder is more visible at this energy than for the average trial, and because the density fit drops this a bit lower than the temperature fit, it maintains the quiescent slope better.

The flaring trials are, at first glance, quite poor. The amount of change in index to the flaring spectrum is much more noticeable than to the quiescent spectrum. Again, the bremsstrahlung cutoff plays a large role in these fits. Turning up the temperature does not get the bremsstrahlung slope up to the flaring spectrum, but turning up the density does. Because of this, it can be seen that a small change in density can yield a large change in X-ray spectral index. Specifically, the lower energy spectrum for the flaring X-ray density fit has a much higher index, while the higher energy portion has an index quite close to the flaring spectrum.

In general, the fits by changing density are better at fitting the quiescent and flaring data spectra, largely due to the fact that the extreme index changes to the flaring spectrum can be explained by the presence of the bremsstrahlung bump. The other spin values considered, $a/M = 0.65$, 0.8, and 0.99, yielded similar results to the previous trials. Most noticeable in each case is that the density fits are significantly better than the temperature fits, suggesting again that accretion rate variations may be more reasonable to suggest as the dominant flaring mechanism.

5. DISCUSSION

The sample fits immediately suggest that a density higher than $n = 1 \times 10^7$ cm^{-3} is necessary to yield an adequate fit to the radio, IR, and optical spectra. The $n = 3 \times 10^7$ cm^{-3} runs have some conflict with the *Swift* upper limits in the hard X-ray regime, which restricts the accretion rate to $\dot{m}_{\rm max} = 3 \times 10^{-4}$. These upper limits are only considered for the average *Chandra* X-ray data fits, as they are essentially averages over a number of years.

As it is expected that a larger simulation volume for the accretion flow would only add significantly to the bremsstrahlung flux, $n = 3 \times 10^7$ cm^{-3} can be seen as an upper limit to the density maximum. This is because of the artificial initial condition of a small-radius torus, rather than near Bondi-scale accretion.

The details of the average X-ray fit benchmark MC trials are shown in Table 2. These include the physical parameters of the runs (electron temperature, density, and magnetic field), *Chandra* spectrum fit, and data and model spectral indices.

As discussed above, we focus on the $n = 3 \times 10^7$ cm^{-3} trials as these gave the best fits to radio–IR–optical data. There are four different spin rates to consider: $a/M = 0.65$, the lower limit suggested in literature, 0.8, 0.9, and 0.99, a near-maximally rotating black hole. The fits to *Chandra* spectra do not allow much differentiation between these trials, as they yield very similar results. Spectral indices range from $\alpha = 0.85$ to 0.92, close fits to the *Chandra* given 0.92.

Table 2
Table of Model Average X-ray Fits for $n = 3 \times 10^7$ cm^{-3}

Label	Spin (a/M)	Magnetic Field	Field Scaling[a]	Temperature	Density	Fit to:	*Chandra* Index[b]	Model Index[b]
1	0.65	2000 G	62.5	15 MeV	3×10^7 cm^{-3}	Average	0.92 ± 0.044	0.90
2	0.8	2600 G	47.3	20 MeV	3×10^7 cm^{-3}	Average	0.92 ± 0.044	0.85
3	0.9	500 G	6.1	22 MeV	3×10^7 cm^{-3}	Average	0.92 ± 0.044	0.92
4	0.99	460 G	2.9	7 MeV	3×10^7 cm^{-3}	Average	0.92 ± 0.044	0.86

Notes. The indices shown are in the energy band from 0.2 to 6 keV, both for *Chandra* data and model fits. Magnetic field, electron temperature, and electron density values given are the maximum for each within the simulation grid, which all other cells scale to.
[a] This value is the factor the GRMHD MRI-saturated magnetic field had to be scaled by to appropriately normalize MC output, as discussed in the text.
[b] Index α for a power-law fit: $F_\nu \propto \nu^{-\alpha}$.

Table 3
Table of Model Flaring/Quiescent X-ray Fits for $n = 3 \times 10^7$ cm^{-3}

Label	Spin (a/M)	Scaling Factor	Fit to:	Fit by:	*Chandra* Index[a]	Model Index[a]
5	0.65	0.87	Quiescent	Temperature	1.08 ± 0.062	0.67
6	0.8	0.75	Quiescent	Temperature	1.08 ± 0.062	0.55
7	0.9	0.86	Quiescent	Temperature	1.08 ± 0.062	0.70
8	0.99	0.80	Quiescent	Temperature	1.08 ± 0.062	0.64
9	0.65	0.83	Quiescent	Density	1.08 ± 0.062	0.80
10	0.8	0.77	Quiescent	Density	1.08 ± 0.062	0.99
11	0.9	0.83	Quiescent	Density	1.08 ± 0.062	0.88
12	0.99	0.77	Quiescent	Density	1.08 ± 0.062	0.87
13	0.65	1.13	Flaring	Temperature	0.64 ± 0.035	0.99
14	0.8	1.25	Flaring	Temperature	0.64 ± 0.035	1.00
15	0.9	1.14	Flaring	Temperature	0.64 ± 0.035	1.02
16	0.99	1.19	Flaring	Temperature	0.64 ± 0.035	1.03
17	0.65	1.22	Flaring	Density	0.64 ± 0.035	0.93
18	0.8	1.33	Flaring	Density	0.64 ± 0.035	0.84
19	0.9	1.20	Flaring	Density	0.64 ± 0.035	0.94
20	0.99	1.27	Flaring	Density	0.64 ± 0.035	0.89

Notes. The scaling factor given is the factor either the electron temperature or electron density is multiplied by from the average benchmark fit (see Table 2) to get a new value for the quiescent or flaring fit presented.
[a] Index α for a power-law fit: $F_\nu \propto \nu^{-\alpha}$.

Also of interest in Table 2 are the specific parameters required for fits. The general trend is that lower spin runs require higher electron temperatures and magnetic fields to match appropriate spectral properties. HARM runs conducted to test the response of the simulation to additional primordial toroidal fields have shown that the MRI development is approximately the same (with higher final field values) for field scaling up to an order of magnitude. Beyond this, the large magnetic pressure dominates the simulation, inhibiting accretion. This allows an easy evaluation of the average fit models, as the 0.65 and 0.8 spin runs require much higher field scaling, while the 0.9 and 0.99 trials are more reasonable.

5.1. Flaring and Quiescent Fits

Table 3 details quiescent and flaring spectral fits, as well as describing the change necessary for each fit, from the benchmark average fits, for each spin value. The 0.65 and 0.8 trial details are included for completeness, but will not be discussed extensively. As mentioned previously, their magnetic field scaling values suggest that they may not be reasonable spin values, and the qualitative analysis is very similar to that of higher spin rate trials.

The quiescent spectrum is very close in spectral index to the average spectrum. It can be fairly easily fit by decreasing density from the average fit's parameters. Lowering temperature yields a slightly less satisfactory fit at the quiescent spectrum, with a spectral index too low and spectrum too hard. For every trial conducted, regardless of spin, the density fits showed closer fits to *Chandra* data (with quiescent spectral index $\alpha = 1.08$) than the temperature fits. Specifically, the 0.99 spectrum (benchmark $\alpha = 0.86$) became slightly softer ($\alpha = 0.87$) as expected for the density adjustment, while scaling temperature led to a harder spectrum ($\alpha = 0.64$). The 0.9 spectrum (benchmark $\alpha = 0.92$) became harder with density scaling ($\alpha = 0.88$), but this is still significantly better than the temperature-adjusted trial ($\alpha = 0.70$).

Flaring fits are more complicated to achieve. Because the spectral index is quite a bit lower than that of the average fit—and the change between indices is much greater than between the average and quiescent—it is nearly impossible to fit the flaring spectrum by simply adjusting one parameter. However, the fact that the bremsstrahlung emission is visible here, whereas it was not in the lower density trials, means that density changes can have a large impact on where in the energy band the change from Compton spectrum to bremsstrahlung spectrum occurs. At this density, $n = 3 \times 10^7$ cm^{-3}, the bremsstrahlung spectrum dominates at an energy around several keV. Therefore, when the density is increased, and the bremsstrahlung component is increased more than the Compton component, the bremsstrahlung emission is visible down closer to 1 keV.

To demonstrate, the bremsstrahlung spectrum above 1 keV (for the run with $n = 3 \times 10^7$ cm^{-3}, $a/M = 0.9$, average fit) much better describes the hard index at the flaring spectrum than the softer Compton spectrum. Specifically, a power-law fit from 0.2 to 1 keV has an index $\alpha = 1.13$, while a fit from 1 to 6 keV has an index $\alpha = 0.69$. Fitting the full range from 0.2 to 6 keV yields an index $\alpha = 0.92$. These compare to *Chandra* X-ray spectral indices of 1.08 for the quiescent spectrum, 0.64 for flaring, and 0.92 for average. As the *Chandra* X-ray data range from 0.2 to 6 keV, it is clear that small changes in parameters could lead to any of the three of these fits being appropriate throughout the range.

None of the fits shown exactly traces the flaring spectrum, but it is simple to see that the density variations work better than temperature variations, and the density fits show promise at slightly higher energies to fitting the flare spectral index. Quantitatively, the *Chandra* flaring data (with spectral index $\alpha = 0.64$) are better fit by density changes ($\alpha = 0.94$, 0.89 for spin 0.9, 0.99) than by temperature changes ($\alpha = 1.02$, 1.03 for spin 0.9, 0.99). For both spin rates, density fits are more consistent with data.

5.2. Model Tests and Evaluation

With both flaring and quiescent spectra better fit from the average spectrum by density changes, it is worth considering how much the density has to be changed for these fits. From the starting density of $n = 3 \times 10^7$ cm^{-3}, the quiescent spectrum was best fit with an average of $n = 2.4 \times 10^7$ cm^{-3}. Similarly for the flaring spectrum, an average of $n = 3.7 \times 10^7$ cm^{-3} was required. This suggests changes in accretion rate, from the average fit, of about 20%–25%. As discussed previously in Hilburn et al. (2010), mass accretion rates vary in HARM trials by about a factor of two. Similarly, Dexter et al. (2009, 2010) suggest variability up to about 50% for both 2D and 3D Sagittarius A* models. Both of these examples comfortably allow for the density variations required for fits.

Following Moscibrodzka et al. (2011), we consider the size of the 230 GHz photosphere from our models, to compare to Very Long Baseline Interferometry (VLBI) measurements by Fish & Doeleman (2010) which found structure at this frequency on the scale of several Schwarzschild radii. All four spin trials had photospheres within 10 M, with higher spin trials having smaller photospheres, as expected. Clearly, accretion flow models are consistent with current VLBI results.

The assumption that radiative cooling is unnecessary in the GRMHD calculation is motivated by the flow being radiatively inefficient. The typical 0.9 spin average run has a radiative efficiency of $\eta \approx 10^{-2}$, an order of magnitude less than the canonical value $\eta \approx 10^{-1}$ for an efficient thin disk.

Based on the trials done, there is little to choose between the different spin rates considered. The 0.9 and 0.99 runs are more likely than lower spin trials due to the primordial magnetic fields required. Of these, the 0.9 run may be marginally better at low energies, but not definitively so. On the other hand, the density changes are definitely better than the temperature changes, suggesting that changes in accretion rate are most likely to explain flaring behavior, based on these trials.

6. SUMMARY AND CONCLUSIONS

In order to explore flaring mechanisms at play in M87's core, full trials have been conducted using a GRMHD accretion evolution scheme, to solve for global physical parameters, and a novel MC radiation transport code, to generate spectra from these parameters. The flaring data being displayed are in *Chandra*'s X-ray band. Trials are fit to an average X-ray spectrum, and then changes necessary to fit quiescent and flaring X-ray spectra are discussed, along with ramifications of specific changes.

To evaluate likely spin rates, with literature suggesting $a/M \geqslant 0.65$, four different GRMHD runs are used, with $a/M = 0.65$, 0.8, 0.9, and 0.99. Articles also suggest an accretion rate under $\dot{m} = 1.6 \times 10^{-3}$, but above or around $\dot{m} = 1 \times 10^{-4}$. To take this into account, the maximum density assigned was adjusted to provide sets of runs at $\dot{m}_{\rm max} \approx 3 \times 10^{-5}$, 1×10^{-4}, and 3×10^{-4}.

Only the highest accretion rate trials, which correspond to a maximum density of $n = 3 \times 10^7$ cm^{-3}, manage to fit lower energy data adequately, and so were focused upon for fitting the flaring X-ray spectrum. This density also shows that higher average accretion rates are unlikely, as the bremsstrahlung emission is very close to upper limits provided by the *Swift* hard X-ray data. As including larger volumes can only maintain or raise the bremsstrahlung flux, this places an upper limit on maximum density and accretion rate.

Quiescent and flaring fits were presented which require only changing density or temperature from the average fits. This can simulate either a global accretion rate change or a global electron temperature change—indicative of more efficient electron heating. During none of these trials was the magnetic field changed in fitting quiescent and flaring spectra, in order to isolate the parameter changes.

The quiescent X-ray spectrum has a very similar spectral index to the average X-ray spectrum. Because of this, it is fairly simple to get a close fit by simply dropping either temperature or density from the average spectrum. In general, no spin rate stands out as having outstanding quiescent fits. They all exhibit similar behavior: the density-changed trials have a slightly better index, while the temperature-changed trials are a bit too hard at the quiescent spectrum.

The flaring spectrum is more difficult to explain. Unlike the quiescent spectrum, the flaring spectrum's index is substantially harder than that of the average spectrum, suggesting a much harder spectrum. Again, no spin rate displays perfect fits. These actually look worse than the quiescent fits, because in order to explain both the slope and flux changes, the bremsstrahlung bump has to be enhanced. This leads to a transition between Compton and bremsstrahlung dominance essentially right at the X-ray data, so that small changes can lead to the X-ray points falling on either side of this transition. In general, the higher energy (bremsstrahlung) side of the X-ray runs seems to adequately describe the index at the flaring spectrum, while the lower energy (Compton bumps) side traces the average and quiescent spectra well, but this is very parameter-sensitive.

Overall, the $a/M = 0.9$ and 0.99 spin runs are marginally better than lower spins at fitting all three X-ray spectra considered, and the $n = 3 \times 10^7$ cm^{-3} trials were the only ones which provided a good fit to radio–IR data at all. This suggests that a maximum accretion rate $\dot{m}_{\rm max} \leqslant 3 \times 10^{-4}$ and spin of $a/M > 0.8$, both well within limits established in literature, are the most appropriate for the core of M87. Scaling between the average X-ray spectrum and flaring and quiescent spectra requires only simple changes in accretion rate (≈20%).

It may be important to note that the higher spin trials have the most prominent polar outflows and show significantly more emission from this assumed jet base than lower spin rates. These

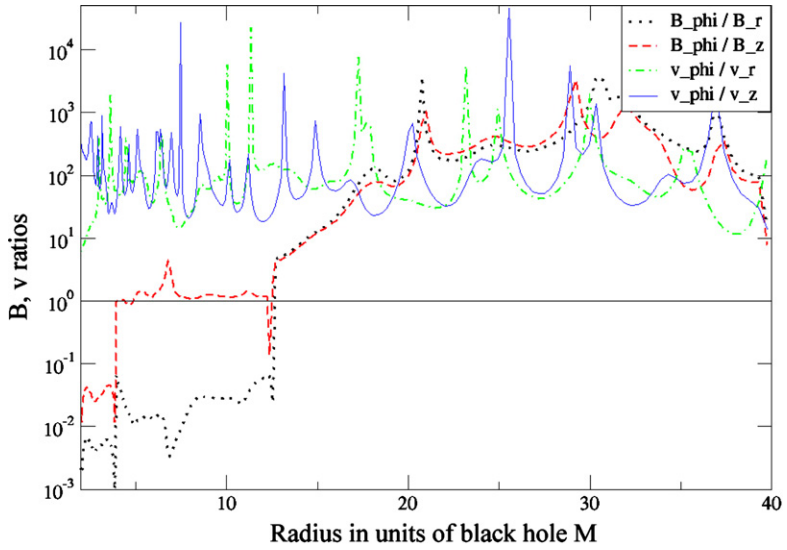

Figure 9. Ratios of components of magnetic field and velocity for a HARM GRMHD run of black hole spin $a/M = 0.99$. The line at unity emphasizes the high degree of anisotropy in these components.

(A color version of this figure is available in the online journal.)

trials are entirely thermal, though jet emission is likely to be nonthermal, and as Dexter et al. (2011) show, the core spectrum can also be fit with nonthermal jet-dominated or jet-and-disk models.

Future modeling work on this source will focus both on more detailed fits of the data already considered and fits including *Fermi* and VHE data, which was not used in this paper. Continued observations of M87 by *Chandra* and *Swift*, which can be used to confirm the trend seen in flux versus index, can help to prove the validity of this work. Specifically, observation of two clear trends can show that the bremsstrahlung and Compton components do both need to be included to fit the flaring spectrum depicted.

Furthermore, more accurate and consistent electron-heating mechanisms, involving PIC simulation results, should lead to better-described electron distributions. Recent results have suggested that particle acceleration by magnetic reconnection in similar situations to MRI disks display a dual Maxwellian nature—with one major population at a low energy and a higher temperature second population. As the spectral indices already considered should be fairly appropriate extended to the VHE regime, this seems quite promising to describe the spectrum more completely. However, since the *Fermi*-VHE spectral index is softer than the *Chandra* X-ray index, any additional nonthermal electron component invoked to model those high-energy data will not impact the thermal spectral fitting to the lower energy data performed here.

G.L.H. specially thanks Xuhui Chen, Dan Harris, and Francesco Massaro, for beneficial discussion and sharing of techniques and observations.

Both authors are also indebted to the anonymous referee, whose thoughtful comments and questions have made a significant impact on the content and quality of this work.

APPENDIX

MONTE CARLO CODE MODIFICATIONS

Data from HARM suggest two shortcomings to the MC code, namely, the anisotropy in velocity and magnetic field. As shown in Figure 9, for a typical run of $a/M = 0.99$, the components of these parameters are usually very disparate. This will obviously lead to highly anisotropic synchrotron radiation and scattering characteristics, for adequately high fields and velocities. The MC code previously considered synchrotron emission as angle-independent and did not allow for relativistic beaming, boosting, and scattering. In order to create a tool as consistent as possible for a number of astrophysical sources, these issues needed to be addressed in the MC code.

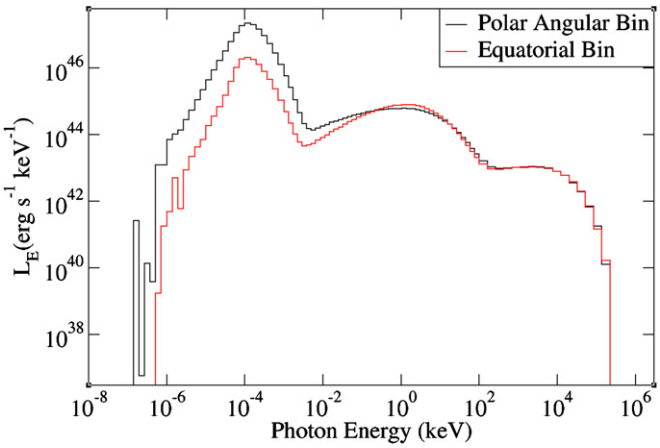

Figure 10. Trial of the anisotropic magnetic field modifications. This is a single-zone run with nearly purely radial field, to best show the effect of the changes. As expected, the synchrotron emission is strongly anisotropic, while the Compton components are much more isotropized.

(A color version of this figure is available in the online journal.)

A.1. Anisotropic Magnetic Field

For fields of the magnitude expected in AGN accretion disks, the dominant effect is on the direction of emission of synchrotron radiation. By Petrosian (1981) the emission scales as $e^{-(\nu/\nu_b)[(4.5/\sin\theta)(\nu_b/\nu kT)^2]^{1/3}}$ for semi-relativistic temperatures and $((1+\cos^2\theta)/\sin^2\theta)e^{-(\nu/\nu_b)ln(2\nu_b/e\nu kT\sin^2\theta)}$ for non-relativistic temperatures, where ν is the photon frequency, $\nu_b = eB/2\pi m_e c$ is the gyrofrequency, B is the magnetic field, T is the electron

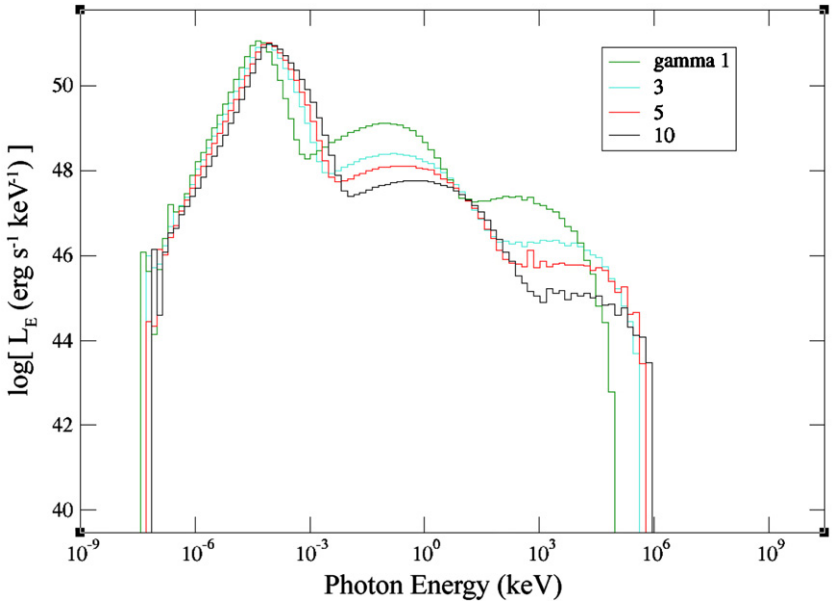

Figure 11. Single-zone trial to illustrate the effects of the suite of velocity modifications. The general effect of higher Lorentz factor (gamma) can be seen in the boosting to higher energies, but the loss of scattering frequency, as photons are beamed in the direction of electron travel.
(A color version of this figure is available in the online journal.)

temperature, and θ is the angle between photon travel and field direction. In an accretion disk, the toroidal magnetic field is often highly dominant. The impact is that photons are emitted strongly perpendicular to this direction.

To best depict the effect, Figure 10 shows a run with a nearly purely radial magnetic field. This results in a much larger number of photons emitted perpendicular to rather than parallel to fields, which leads to a greater flux in the polar direction than the equatorial direction.

A.2. Anisotropic Velocity Field

As the impact will be seen in both emission and scattering events, the process of including plasma flow velocity requires changes to several of the MC code's routines.

1. All emission is beamed in the direction of relativistic plasma flow, and Doppler boosted, with $\cos\phi' = (\cos\phi - (v/c))/(1 - (v/c)\cos\phi)$ and $\nu' = \nu(1 - (v/c)\cos\phi)/\sqrt{1-(v/c)^2}$, where ϕ is the angle between the photon and bulk flow directions, ν is the photon frequency, v is the bulk flow magnitude, and $'$ represents the bulk flow frame.
2. Compton scattering frequency increases when photons travel against the flow of particles (head-on) and decreases when moving with the flow (tail-on), as $f' = f(1 - (v/c)\cos\phi)$, with f representing the scattering frequency.
3. Change in photon energy and direction for scattering events are significantly greater for head-on photons, and vice versa, as the electron distribution is not isotropic in the black hole rest frame, by $\tan\theta' = u\sin\theta/\gamma(u\cos\theta + v)$, where γ is the electron's Lorentz factor, u is the electron velocity, and θ is the respective electron angle of travel.

These effects, taken together, typically result in emissions that are stronger when initially emitted, but have somewhat lower scattering luminosities, as most photons will be beamed in a similar direction to the bulk flow, so will scatter less frequently and with less change in angle. This can be seen in Figure 11, which depicts single-zone trials.

REFERENCES

Abdo, A. A., Ackermann, M., Ajello, M., et al. 2009, ApJ, 707, 55
Acciari, V., Aliu, E., Arlen, T., et al. 2010, ApJ, 716, 819
Acciari, V., Beilicke, M., Blaylock, G., et al. 2008, ApJ, 679, 1427
Aharonian, F., Akhperjanian, A., Beilicke, M., et al. 2003, A&A, 403, L1
Aharonian, F., Akhperjanian, A., Beilicke, M., et al. 2004, A&A, 421, 529
Aharonian, F., Akhperjanian, A. G., Bazer-Bachi, A. R., et al. 2006, Science, 314, 1424
Ajello, M., Costamante, L., Sambruna, R. M., et al. 2009, ApJ, 699, 603
Ajello, M., Rau, A., Greiner, J., et al. 2008, ApJ, 673, 96
Biretta, J., Sparks, W., & Macchetto, F. 1999, ApJ, 520, 621
Biretta, J., Stern, C., & Harris, D. 1991, AJ, 101, 1632
Boettcher, M., & Liang, E. P. 2001, ApJ, 552, 248
Canfield, E., Howard, W. M., & Liang, E. P. 1987, ApJ, 323, 56
Chen, X., Fossati, G., Liang, E. P., & Böttcher, M. 2011, MNRAS, 416, 2368
Cheung, C. C., Harris, D. E., & Stawarz, L. 2007, ApJ, 663, L65
Despringre, V., Fraix-Burnet, D., & Davoust, E. 1996, A&A, 309, 375
Dexter, J., Agol, E., & Fragile, P. 2009, ApJ, 703, 142
Dexter, J., Agol, E., Fragile, P. C., & McKinney, J. C. 2010, ApJ, 717, 1092
Dexter, J., McKinney, J., & Agol, E. 2011, arXiv:1109.6011
di Matteo, T., Allen, S. W., Fabian, A. C., Wilson, A. S., & Young, A. J. 2003, ApJ, 582, 133
Finke, J. D., & Boettcher, M. 2007, ApJ, 667, 395
Fish, V., & Doeleman, S. 2010, 38th COSPAR Scientific Assembly, 2303
Gammie, C. F., McKinney, J. C., & Toth, G. 2003, ApJ, 589, 44
Gebhardt, K., & Thomas, J. 2009, ApJ, 700, 1690
Goldston, J., Quataert, E., & Igumenshchev, I. 2005, ApJ, 621, 785
Hardee, P. 2010, arXiv:1007.0426
Harris, D., Cheung, C., & Stawarz, L. 2009, ApJ, 699, 305
Hilburn, G., Liang, E., Liu, S., & Li, H. 2010, MNRAS, 401, 1620
Levinson, A., & Rieger, F. 2011, ApJ, 730, 123
Li, Y., Yuan, Y.-F., Wang, J.-M., Wang, J.-C., & Zhang, S. 2009, ApJ, 699, 513
Liang, E. P. 2009, arXiv:0902.4740
Liang, E. P., & Dermer, C. D. 1988, ApJ, 325, L3
Liu, W., Li, H., Yin, L., et al. 2011, Phys. Plasmas, 18, 052105
Mei, S., Blakeslee, J. P., Côté, P., et al. 2007, ApJ, 655, 144
Moscibrodzka, M., Gammie, C. F., Dolence, J. C., & Shiokawa, H. 2011, ApJ, 735, 9
Moscibrodzka, M., Gammie, C. F., Dolence, J. C., Shiokawa, H., & Leung, P. K. 2009, ApJ, 706, 497
Narayan, R., & Yi, I. 1994, ApJ, 428, L1
Neronov, A., & Aharonian, F. 2007, ApJ, 671, 85
Noble, S., Gammie, C. F., McKinney, J. C., & Del Zanna, L. 2006, ApJ, 641, 626
Ohsuga, K., Kato, Y., & Mineshige, S. 2005, ApJ, 627, 782

Perlman, E. S., Biretta, J. A., Sparks, W. B., Macchetto, F. D., & Leahy, J. P. 2001, ApJ, 551, 206
Perlman, E. S., Harris, D. E., Biretta, J. A., Sparks, W. B., & Macchetto, F. D. 2003, ApJ, 599, L65
Perlman, E. S., Mason, R. E., Packham, C., et al. 2007, ApJ, 663, 808
Petrosian, V. 1981, ApJ, 251, 727
Rieger, F., & Aharonian, F. 2008, Int. J. Mod. Phys. D, 17, 1569
Shcherbakov, R., & Baganoff, F. 2010, ApJ, 716, 504
Wang, J.-M., Li, Y.-R., Wang, J.-C., & Zhang, S. 2008, ApJ, 676, 109
Wilson, A. S., & Yang, Y. 2002, ApJ, 568, 133
Yuan, F., Quataert, E., & Narayan, R. 2003, ApJ, 598, 30
Zenitani, S., & Hoshino, M. 2005, ApJ, 618, 111
Zenitani, S., & Hoshino, M. 2007, ApJ, 670, 702